Electrolyte Structure with Explicit Solvent in Nanoslit Capacitors using Classical Density Functional Theory

by

James H. Zhang

Submitted to the
Department of Mechanical Engineering
in Partial Fulfillment of the Requirements for the Degree of

Master of Science in Mechanical Engineering

at the

Massachusetts Institute of Technology

September 2021

Signature of Author: _____

Department of Mechanical Engineering
August 6, 2021

Certified by: _____

Xuanhe Zhao
Professor of Mechanical Engineering
Thesis Supervisor

Accepted by: _____

Nicolas Hadjiconstantinou
Professor of Mechanical Engineering
Chairman, Department Committee on Graduate Theses

Electrolyte Structure with Explicit Solvent in Nanoslit Capacitors using Classical Density Functional Theory

by

James H. Zhang

Submitted to the
Department of Mechanical Engineering
in Partial Fulfillment of the Requirements for the Degree of

Master of Science in Mechanical Engineering

ABSTRACT

Understanding the effects of double layer formation on charged interfaces is integral in many disciplines such as electrochemistry, polymer science, and solution theory. Classical models to understand double layer thermodynamics is typically based on the Poisson-Boltzmann equation where solvent is treated implicitly as a dielectric background and ions are treated as point charges. Although this theory works well for macroscopic charge distributions, it is known to lead to problems in nanopores when finite size and interfacial effects play important roles. The advent of using nanoporous electrodes for increased surface interactions motivates us to build a more accurate model that can characterize electrolyte structure in nanoconfined regions.

This theses aims to understand the electrolyte structure and the effects of explicit solvent in nanopores through computations. We first start by giving a brief description on classical models in understanding the behavior of solvent and ions under external electric fields. We then elucidate the problems with these classical models when considering electrolyte structure in nanoconfined regions. Afterwards we give a discussion on classical density functional theory and a method to model three component electrolyte with steric interactions and mean-field electrostatics. This method allows us to construct a local relative permittivity that is a function of the molecular interactions. Using this model, we study the effects of solvent properties, temperature, surface charge, and slit geometry on the adsorption and structure of each component. This model can be used to help guide the design of capacitor systems and understand the underlying thermodynamics of confined double layer formation.

Thesis supervisor: Xuanhe Zhao
Title: Professor of Mechanical Engineering

Acknowledgements

I would like to thank my advisor Professor Xuanhe Zhao for his guidance and welcoming me into the Zhao lab to continue my research. I would also like to thank Professor Gang Chen for his insights, advising, and continued insights for this project. I also thank Professor Evelyn Wang for her leadership and assistance with navigating through the many challenges over the last few months. I am also grateful for the support and kindness offered from my lab mates at the NanoEngineering group, especially Dr. Jiawei Zhou, Qichen Song, and Simo Pajovic for their helpful discussions. I would also like to thank Ms. Keke Xu for her help in the laboratory. Finally, I would like to thank my family and friends for giving me strong support during the first phase of my graduate career.

Table of Contents

List of Figures

List of Tables

Chapter 1: Introduction

The nexus of water and energy is a critical field due to the effects of climate change on natural resources. Although water is one of the most common and important material for society, many of its fundamental properties are still heavily researched due to its interesting behaviors. Water is a commonly used solvent for electrolytes due to its high solvation ability, leading to many interesting phenomena and applications in devices such as in thermally regenerative electrolyte systems [3], [4].

Water's ability to interact with ions and electrostatic fields is due to its high permanent dipole moment. Many of water's unique properties, such as high relative permittivity and hydrogen bonding structure, is related to its directional electrostatic interactions. Although water's unique electrostatic properties are well known, their thermodynamic behaviors are commonly ignored in classical electrostatic solution models to simplify equations. Poisson-Boltzmann equation, perhaps the most famous electrostatic equation in solution chemistry, only treats water as a passive background dielectric material when calculating charged species' distributions. This assumption is reasonable for macroscopic density distributions in the presence of weak electric fields, where the majority of water molecules display bulk behavior. This assumption fails when nanoscale and interfacial effects play a dominating role and causes the water molecules to deviate from bulk behavior. Nanoporous electrodes can cause this due to confinement effects in their hierarchical pore structures.

In this chapter, we first present a motivation on why understanding solvent behavior is important for designing new devices. A review on classical electrostatic theories for solution chemistry will then be presented to understand their developments. Finally, a discussion will be given on this thesis's work.

1.1 Motivation for Polar Solvent Thermodynamics

Polar solvents and electrolytes can re-arrange themselves when in contact with charged surfaces to minimize their electrostatic energies. If there are free ions in the solution, then it will form an ionic double layer screened by the solvent. Double layers occur in many systems such as

on colloid surfaces[5], [6], hydrogels [7], and electrochemical systems[8], [9]. In particular for electrochemical systems, understanding the thermodynamics of double layers is crucial for designing high performance devices. The double layer's charge distribution directly impacts the amount of energy a capacitor can store [8], [10].

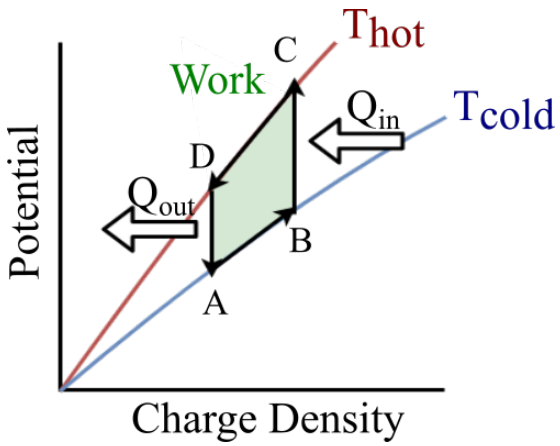

Figure 1-1: Schematic of thermodynamic cycle in thermocapacitor to extract work from temperature dependent behaviors of double layers in capacitor systems.

Manipulating the thermodynamics of the double layer has allowed the development of new devices that can extract electrical power from waste heat using changes in system entropy [3], [4]. A thermodynamic cycle is constructed by using the temperature dependent electrode potential due to changes in the double layer structure as shown in Figure 1-1. First, the system is charged at a low temperature from point A to B. Afterwards, the capacitor is heated at open circuit using waste heat to a higher temperature at point C. The cell potential will increase due to re-arrangements of the structure in the double layer. The cell is then discharged to point D. Finally, the cell is cooled down back to point A to complete the cycle. The total area enclosed by this cycle is related to the work done. Theoretical efficiencies predict between 4% to about 10% efficiency for a temperature difference of 50 K and heat recuperations of 80% [4]. Many models used to understand experimental data is based on classical macroscopic models such as Poisson-Boltzmann equation due to their simplicity and elegance; however, these models are unlikely to capture all of the thermodynamics correctly because of the negligence of solvent effects. Coulometric and calorimetric measurements were made on carbon electrodes to understand temperature effects on the electric double layer [11]. Their measurements showed that entropic effects account for

approximately 25% of the total grand potential energy at high potentials in contrast to 100% predicted by the diffuse model from Poisson-Boltzmann [12].

Another important effect in modern electrodes are confinement effects due to nanoporous electrodes. Electrodes are commonly made with porous materials due to their high specific surface area for improved kinetics and charge storage [13]. Nanoporous carbon electrodes have pore sizes on the order of 1 nm, which is comparable in size with the diameters of both solvent and ions. Nanopores have been shown to violate common assumptions made in macroscopic models, such as electroneutrality. NMR measurements on carbon based electrodes have showed that electroneutrality is not preserved inside of nanoconfined regions depending on ion-specific interactions [14]. Nanoconfined regions can also cause overlapping double regions between parallel walls, leading to net charges [15]. The coupled electrostatic and wall interactions between double layers could also lead to interesting solvent interactions that are not well investigated.

1.2 Theory of Dielectric Solutions

The theory of dielectrics can be most easily understood using a simple parallel capacitor plate. First consider the case where the parallel plates have opposite electrical surface charge densities with only vacuum in between. The electric field, $\underline{\nabla\phi}$, will then be constant and proportional to the surface charge density. If a dielectric material with relative permittivity ϵ_r is inserted in between the capacitor plates, then a polarization field $\underline{P}$ will form due to work from the electric field. The sum of these two components give rise to the displacement field

$$\underline{P} = \chi\epsilon_0\underline{E} \qquad \text{Eq. 1.2.1}$$

$$\underline{D} = \underline{\nabla}\phi\epsilon_0 + \underline{P} = \underline{\nabla}\phi\epsilon_0\epsilon_r \qquad \text{Eq. 1.2.2}$$

By re-arrangement of Eq. 1.2.1 and 1.2.2 and recognizing that the polarization field is in the same direction as the electric field, then a simple relationship can be found between the polarization field and the relative permittivity of a material.

$$\chi = \epsilon_r - 1 = \frac{P}{\epsilon_0\nabla\phi} \qquad \text{Eq. 1.2.3}$$

It is important to note that in this work, we will always be referring to the material's static relative permittivity rather than a frequency dependent permittivity. Water in particular has a very high relative permittivity at 78.3 [2] in room temperature due in part to its large permanent dipole

moment. Water molecules can rotationally re-orient themselves in the presence of electric fields to minimize their free energy from electrostatics. Classical mean field theories to predict dielectric solution thermodynamics have been extensively researched to predict their bulk relative permittivity using only molecular information.

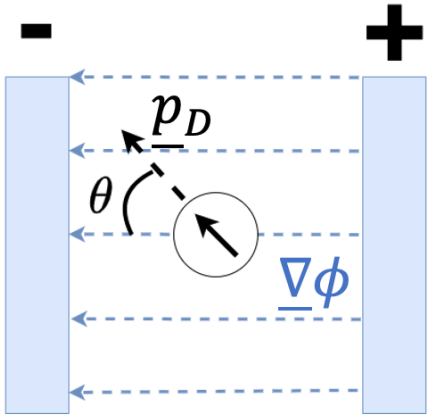

Figure 1-2: Schematic of the orientation of a dipole with respect to an external electric field.

Debye theory for dielectrics was one of the first theories applicable to dilute polar fluids [16]. Key assumptions in this derivation are that the electric field is weak and that dipoles are non-interacting. An electric field will both rotate a polar molecule and elastically displace the molecule's electrons. The electrostatic energy of the dipole due to rotation is

$$u = -p_D \nabla\phi cos\theta \qquad \text{Eq. 1.2.4}$$

where u is the electrostatic energy, p_D is the dipole moment of the molecule, and θ is the relative angle formed between the molecular dipole vector and the electric field. Using classical Boltzmann distribution, the average angle of a dipole gas in an electric field can be calculated.

$$< \cos\theta > = \frac{\int cos\theta \exp(\beta p_D E cos\theta)\, sin\theta d\theta}{\int \exp(\beta p_D E cos\theta)\, sin\theta d\theta} = \coth(\beta p_D E) - \frac{1}{\beta p_D E} \qquad \text{Eq. 1.2.5}$$

where β is $\frac{1}{k_B T}$ and the angle bracket represents a thermodynamic average. The resultant function is commonly known as the Langevin function.

$$L(Z) \equiv \coth(Z) - \frac{1}{Z} \qquad \text{Eq. 1.2.6}$$

In the presence of weak electric field where $Z \ll 1$, $L(Z)$ can be Taylor expanded to the first order term $\frac{Z}{3}$. Thus, the total average moment of a dipole in the Debye model is

$$p_{tot} = \frac{\beta p_D^2 E}{3} + \alpha \qquad \text{Eq. 1.2.7}$$

where α is the polarizability of the molecule. Debye then derived a formula to calculate the dielectric's relative permittivity by using the Clausius-Mossoti relation [16]

$$\frac{\epsilon_r - 1}{\epsilon_r + 2} = \frac{\rho_D}{3\epsilon_0}\left(\alpha + \frac{\beta p_D^2}{3}\right) \qquad \text{Eq. 1.2.8}$$

where ρ_D is the dipole number density. It is clear that the assumptions in deriving this equation should underpredict the relative permittivity of strongly interacting dipoles, such as liquid water. Assuming that the molecular polarizability is 0 and the dipole moment is 2.5 D, the calculated relative permittivity is -2.5.

To accurately calculate the relative permittivity of water, the hydrogen bonding network from dipole-dipole correlations needs to be considered. Strong local interactions between neighboring molecules causes their orientations to be influenced by one another rather than just by an external field, leading to a high relative permittivity [9].

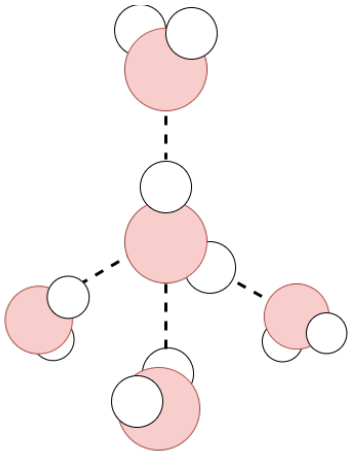

Figure 1-3: Schematic of tetrahedral ordering that water molecules can form due to its local hydrogen bonding from oxygen's lone pairs and hydrogen atoms.

This development was first shown with Onsager's derivation, which took into account long-range dipolar interactions and ignored short-range interactions [17]. Kirkwood took this

derivation another step further by considering short-range interactions in strongly interacting systems [18]. The derivation is quite involved and will not be detailed here. The final equation Kirkwood derived is

$$\frac{(\epsilon_r - 1)(2\epsilon_r + 1)}{3\epsilon_r} = \frac{\rho_D}{3\epsilon_0}\left(\alpha + \frac{\beta p_D^2}{3} g_K\right) \quad \text{Eq. 1.2.9}$$

where g_K is the Kirkwood correlation factor. The correlation factor equals 1 if there are no correlations and will be greater than 1 if there are correlations. If only nearest neighbors are considered, then the correlation factor can be approximated as

$$g_K = 1 + z < cos\theta_{ij} > \quad \text{Eq. 1.2.10}$$

where z is the number of nearest neighbors and $< cos\theta_{ij} >$ describes the expected relative angle between molecule i and j. By assuming a purely tetrahedral structure, Oster et al calculated a relative permittivity for water at 78.2, which is an extremely good estimate [19]. Some limitations with applying this model is that the Kirkwood correlation factor is not always known a priori and it is difficult to determine accurately for mixtures. Furthermore, the correlation factor should be a function of all molecular interactions such as van der Waals and steric interactions [9].

1.3 Classical Double Layer Theories

It has been widely known that if a charged interface is brought into contact with a solution of dissolved ions, then the ions will re-arrange themselves to form favorable electrostatic interactions. Called the ionic double layer, this structure has been extensively studied due to its wide applications in understanding surface phenomena through classical theories and atomistic simulations [10], [20]–[22]. Classical theories have the benefit of simple interpretation and fast computations at the cost of accuracy. The most famous theories that will be discussed are the Helmholtz model [23], Gouy-Chapman model [24][25], and the Stern model [26].

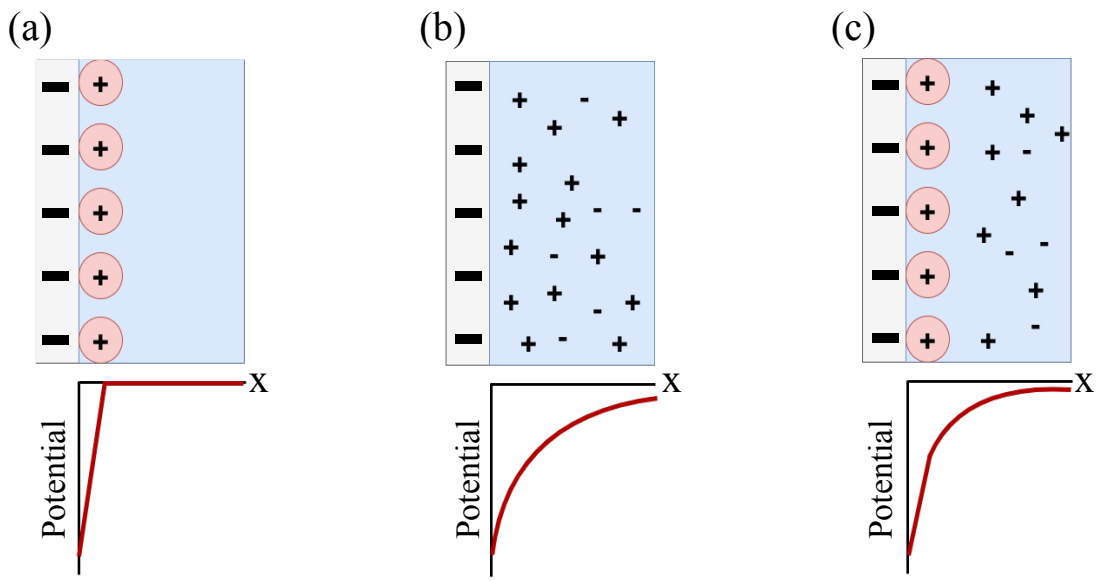

Figure 1-4: Theories for double layers formed by electrolytes against a negative interface using (a) the Helmholtz model, (b) the Gouy-Chapman model, and (c) the Stern model.

Helmholtz was the first one to consider charge separation effects on an electrode surface in 1874 [23]. Recognizing that the excess charge on an electrode will attract ions, he hypothesized that a compact layer of counter-ions will form to balance this charge. A deficiency in this model is that it only predicts linear drop in potential across this layer, giving a constant capacitance only dependent on the thickness of the inner Helmholtz layer and the solvent's relative permittivity. Another key deficiency is that it does not take into account the effects of thermal fluctuations and correlations in ion positions beyond this first layer [9].

Gouy [24] and Chapman [25] both understood that the capacitance would not be constant due to the thermal mobility of ions. Their model developed a diffuse model based on Poisson's equation to predict the charge distribution of ions in the double layer. Assuming that ions are point charges and all interactions are only electrostatic, then the density of ions away from the electrode surface follows a Boltzmann distribution

$$\rho_I = \rho_{bulk,I} \exp(-\beta z_I e \phi) \qquad \text{Eq. 1.3.1}$$

where ρ_I is the density of the ion, I is the index for the ion type, z is the valence charge of the ion, e is the elementary charge, ϕ is the electrostatic potential. Poisson's equation states that the divergence of the displacement field is equal to the ionic charge density

$$\nabla \cdot (\epsilon_r \nabla \phi) = \sum_{I=1}^{N} -\frac{z_I e \rho_I}{\epsilon_0} \quad \text{Eq. 1.3.2}$$

where there are N ionic species. If water is assumed to be only a background dielectric material that shield's electrostatic interactions, then the relative permittivity is constant. This equation can be reduced to the Poisson-Boltzmann equation in the one-dimensional case.

$$\epsilon_r \frac{d^2\phi}{dx^2} = \frac{e}{\epsilon_0} \sum_{I=1}^{N} z_I \rho_{bulk,I} \exp\left(-\frac{z_I e \phi}{k_B T}\right) \quad \text{Eq. 1.3.3}$$

This equation can be solved to calculate the ion distributions in full or linearized in the low potential case using the Debye length [27]. The Debye length, κ^{-1}, is commonly used to characterize the double layer size as a function of simple parameters.

$$\kappa^{-1} = \sqrt{\frac{\epsilon_r \epsilon_0 k_B T}{2e^2 I}} \quad \text{Eq. 1.3.4}$$

where I is the ionic strength of the solution and related to the ionic valence charge and density.

The Gouy-Chapman model predicts an exponential decay in the capacitance and incorporate temperature effects into the double layer theory. A key limitation of this model is the use of point charges, which do not take into account finite size packing effects. This leads to the prediction of ionic densities at the surface of the electrode to be many orders of magnitude larger than what is physically possible.

Stern's model [26] attempted to rectify this by combining elements from Helmholtz's model and Gouy-Chapman. Within the inner layer of counter-ions, he modeled it as specifically adsorbed with a distance of closet approach on the order of ionic radius. Outside of this region is a region of diffuse point charges [9]. This model predicts a linear drop in potential across the inner layer and an exponential decay across the outer layer.

A key component that is missing within all of these models is the active role that water molecules can play in the presence of electric fields. Bockris et al. recognized that water molecules can adsorb onto the electrode with particular orientations, leading to deviations in the double layer's relative permittivity [28]. Bockris treated it as the first layer of solvent having a low relative permittivity due to angular alignment and the second layer of water molecules having a higher relative permittivity. The second layer's relative permittivity was fitted based on experimental values for the first layer's relative permittivity. Marshall and Conway used a lattice-gas model for the adsorbed monolayer of dipoles to calculate the pairwise free energies and their contributions

to its chemical potential [29], [30]. Using this method, they found that dipole-induced dipole interactions can have large effects on the pseudo-capacitance curves.

1.4 Outline of Thesis

The goal of this thesis is to develop a model to study double layer structures in nanoconfined geometries with explicit consideration of polar solvent interactions. In Chapter 1, a brief overview on motivations, classical theories in solution dielectrics, and double layer theory was presented. Chapter 2 will go into detail on classical density functional theory (c-DFT) and the dipolar Poisson-Boltzmann equation to model a primitive three component electrolyte. Discussions will also be presented on limitations of this model and other polar solvent models in literature. Chapter 3 will discuss the numerical methods on how the c-DFT algorithm was implemented in code. Chapter 4 presents the double layer structures calculated for a variety of different scenarios such as different surface potentials, dipole moments, temperatures, and slit widths. Chapter 5 will summarize the findings and identify possible future endeavors in this model.

Chapter 2: Classical Density Functional Theory and Dipolar Poisson-Boltzmann Equation

Classical density functional theory (c-DFT) provides a framework to investigate the properties of inhomogeneous fluids by calculating the minimum of a thermodynamic function. C-DFT was developed in analogue to quantum DFT. Whereas quantum DFT calculates the electron density distribution function and quantum effects, c-DFT calculates the fluid density distribution function. Due to its ability to capture many-body interactions without explicitly tracking the trajectories of individual particles like in molecular dynamics, classical density functional theory has been used extensively to study the adsorption of fluids in confined geometries.

2.1 Classical Density Functional Theory

Fluid adsorption in materials can be modeled as a mixture of a fluid and solid host. If the degrees of freedom for the host material is ignored, then the grand canonical free energy will only be a functional of the fluid density distribution for N fluid components

$$\Omega[\{\rho_i(\underline{r})\}] = \sum_{i=1}^{N} \mathcal{F}_{id}[\{\rho_i(\underline{r})\}] + \mathcal{F}_{ex}[\{\rho_i(\underline{r})\}] + \sum_{i=1}^{N} \int d\underline{r}\rho_i(\underline{r})(V_{ext,i}(\underline{r}) - \mu_i) \quad \text{Eq. 2.1.1}$$

where Ω is the total grand canonical free energy of the system, $\mathcal{F}_{id}$ is the intrinsic kinetic free energy of the system, $\mathcal{F}_{ex}$ is the intrinsic excess free energy, $V_{ext,i}$ is the external wall potential on the i^{th} species, μ_i is the chemical potential of the i^{th} species, ρ_i is the density of the i^{th} species, and $\underline{r}$ is the position vector.

The first term is the kinetic ideal gas component and is known exactly as

$$\mathcal{F}_{id}[\{\rho_i(\underline{r})\}] = \beta^{-1} \int d\underline{r}\rho_i(\underline{r})(\ln(\lambda_i^3\rho_i(\underline{r}) - 1)) \quad \text{Eq. 2.1.2}$$

where λ_i is the thermal de Broglie wavelength of component i. The excess free energy component, $\mathcal{F}_{ex}$, describes the fluid-fluid particle interactions and are usually approximations for different interactions. The chemical potential can also be split into an ideal and kinetic component similar to the excess free energy.

$$\begin{aligned}\mu_i &= \mu_{id,i} + \mu_{ex,i} \\ &= \beta^{-1}\ln\left(\lambda_i^3 \rho_{bulk,i}\right) + \mu_{ex,i}\end{aligned} \qquad \text{Eq. 2.1.3}$$

Similar to quantum DFT, two powerful theorems are used that make it possible to calculate the fluid adsorption properties using c-DFT. The first theorem states that the external potential, and consequentially the grand canonical free energy, is uniquely determined by the equilibrium density distribution. The second theorem states that the equilibrium density profile minimizes the total grand canonical free energy and it can be obtained using the variational principle for the grand potential.

$$\frac{\delta\Omega[\rho_i]}{\delta\rho_i(\underline{r})} = 0 \qquad \text{Eq. 2.1.4}$$

Combining Eq 2.1.1 to 2.1.4 and then solving for $\rho_i(\underline{r})$ for each component gives the final equation.

$$\rho_i(\underline{r}) = \rho_{i,bulk}\exp\left(-\beta V_{ext,i}(\underline{r}) - \beta\frac{\delta\mathcal{F}_{ex}}{\delta\rho_i} + \beta\mu_{ex,i}\right) \qquad \text{Eq. 2.1.5}$$

The second term in Eq. 2.1.5 is the one-body direct correlation term. The excess chemical potential is chosen such that when there is no external potential field, the one-body direct correlation function equals to the excess chemical potential. This leads to the equation to reduce to a homogenous bulk solution where $\frac{\rho_i(\underline{r})}{\rho_{i,bulk}} = 1$.

There is no exact formula for the excess free energy functional, which is crucial to modeling real fluid interactions. Using thermodynamic functional integration [31], it can be found that the total intrinsic free energy is equal to the sum of a reference fluid and a path integrated interaction term

$$\mathcal{F}[\rho] = \mathcal{F}_{ref}[\rho] + \frac{1}{2}\int_0^{\nu} d\nu' \int d\underline{r}_1 \int d\boldsymbol{r}_2 \rho^{(2)}(\nu';\underline{r}_1,\underline{r}_2)u(\underline{r}_1,\underline{r}_2) \qquad \text{Eq. 2.1.6}$$

where $\mathcal{F}_{ref}$ is the reference intrinsic energy, ν is the charging term to go from the reference system to the system of interest, $\rho^{(2)}$ is the two-body density term, and u is the pair-wise interaction term. Higher-order interaction terms are typically ignored, but can be included as well. Eq. 2.1.6 can be thought of as modeling a real fluid by using the interaction term as a perturbation to a reference system. It is difficult to accurately implement the two-body density terms in calculations because of correlation effects [32]. As a result, it is common to implement a mean-field simplification to

the interaction terms. This assumption effectively sets the correlations to 0 at short distances. This occurs in systems naturally when separations between particles are large [33].

$$\rho^{(2)}(\nu';\underline{r}_1,\underline{r}_2) \approx \rho(\underline{r}_1)\rho(\underline{r}_2) \qquad \text{Eq. 2.1.7}$$

By setting ν to 1 and using the mean-field approximation, the starting point to model fluid interactions in classical density functional theory in the mean field can be stated.

$$\mathcal{F}_{ex}[\rho] = \mathcal{F}_{ref,ex}[\rho] + \frac{1}{2}\int d\underline{r}_1 \int d\underline{r}_2 \rho(\underline{r}_1)\rho(\underline{r}_2)u(|\underline{r}_1 - \underline{r}_2|) \qquad \text{Eq. 2.1.8}$$

The negligence of higher order correlation terms may impact the thermodynamics especially in systems with strong correlations such as in water.

2.2 Methods to Model Polar Solvent Thermodynamics in Classical Density Functional Theory

Developing models that can accurately reproduce a wide range of water's properties is a long standing research topic in classical density functional theory. Models for polar solvents in classical density functional theory generally fall into two different categories corresponding to how they treat dipolar interactions. The first type uses an explicit hydrogen bonding term that account for short-range directional bonding. The second type uses explicit electrostatics to account for dipolar interactions. A brief literature review and descriptions on the models will be given to understand the differences in these models.

Explicit hydrogen bonding terms can account for the short-range networks that polar solvents form. Water in particular is known for forming tetrahedral and "ring-and-chain" structures due to its tetrahedral charge distribution [34]. These class of models are largely based on Wertheim's theory of directional attractive forces using graph theory [35]–[38]. His method used geometric arguments and cluster expansions to define the excess free energy terms in associating fluids. Equations of state for associating fluids (SAFT) [39], [40] and inhomogeneous versions of SAFT suitable for density functional theories [41]–[43] have been utilized to study the thermodynamics of associating fluids. A commonly used hydrogen bonding term in SAFT is the hard square-well potential with geometrical constraints

$$U_{assoc} = \begin{cases} -\epsilon_{assoc}, & r_{min} < r_{12} < r_{max};\ \ \theta_1 < \theta_c;\ \ \theta_2 < \theta_c \\ 0, & otherwise \end{cases} \qquad \text{Eq. 2.2.1}$$

where r_{min} and r_{max} correspond to distance criteria and θ_c correspond to angle criteria for bonding. Many different water models have been proposed to study pure liquid thermodynamics [41], [44], [45], and liquid mixtures [46]. These models have been able to accurately reproduce a wide range of properties such as vapor-liquid equilibria and surface tensions in the bulk. A mixture of two-site polar solvent and associating polymer branches were able to reproduce the lower critical solution temperature typical of pNIPAM due to the balance between local hydrogen bonding and long-range Lennard-Jones attraction [47].

A critical question though is the long-range natured of water's electrostatic dipolar interactions and how to correctly account for these interactions without double counting hydrogen bonds. The hydrogen bonding network involved in water has both partial electrostatic and partial covalency attributes. Some models accounted for this by including both long-range dipolar interactions as well as short range hydrogen bonding terms [48]–[50]. These models have shown the ability to predict a wide range of water properties in both the homogenous and inhomogeneous phases. For pure fluids with moderately strong dipolar moments, it is possible to re-map the long-range dipolar interactions onto the Lennard-Jones attraction and an angle averaged potential [44], [51]; however, it is unclear how hydrogen bonding terms transfers towards electrolytes where ionic interactions are dominated by electrostatics. Jeanmairet et al. produced a three-dimensional model of water with both electrostatic interactions and a three-body hydrogen bonding term to enforce some tetrahedral order in the first few solvation shells [52]. Using the partial charge distribution, the structure facture, and k-dependent dielectric constants, this model was able to predict accurate water structures around both organic molecules and monovalent ions.

Other methods to model water-like molecules is by explicitly considering the electrostatic interactions between a hard-sphere dipolar solvent and hard-sphere ions using the mean spherical approximations (MSA). The mean spherical approximation is based on Ornstein-Zernike integral equations to find correlation functions between particles. It has been successfully applied to understanding the thermodynamics of electrolytes with hard sphere charges and hard sphere dipoles [53]–[55]. Inhomogeneous versions of this theory have been applied in c-DFT to study electrolytes on interfaces [20], [56], [57]. Warshavsky and Marucho in particular have developed an in-depth polar-solvation classical density functional theory model to calculate electrolyte behaviors near charged interfaces [57]. MSA goes beyond mean field electrostatics by including short-range correlations between the electrolyte components.

The method that is presented in this thesis is restricted to the mean field approach due to its low computation costs. The model for the electrolyte is also composed of hard sphere ions and hard sphere dipoles. The electrostatic interactions between all species are treated using the dipolar Poisson-Boltzmann equation, which shares similarities to the Debye-Langevin equation and the Langevin-Poisson EQT method in how they treat dipolar electrostatics [58].

2.3 Fundamental Measure Theory for Hard Sphere Repulsion

Hard sphere fluids has been a starting point in fundamental fluids research due to the important effects of steric hinderance. Repulsions due to finite particle sizes lead to the characteristic peaks seen commonly in liquid radial distribution functions [59]. Rosenfeld constructed a theory for hard sphere mixtures that used fundamental geometric properties to describe the interactions between particles and Scaled Particle Theory to describe the thermodynamics [60]. Called fundamental measure theory as a result, this theory led to many simulations on hard sphere fluid structures near external surfaces.

Rosenfeld first constructed the excess free energy term for fundamental measure theory. If it is assumed that terms beyond the second order term is negligible and the second virial coefficient is written in terms of the Mayer-f function, the excess free energy of the system can be written as

$$\beta\mathcal{F}_{ex}[\{\rho_i\}] = -\frac{1}{2}\sum_{i,j}\int d\underline{r}\int d\underline{r}'\rho_i(\underline{r})\rho_j(\underline{r}')f_{ij}(|\underline{r}-\underline{r}'|) \qquad \text{Eq. 2.3.1}$$

where the total interaction is the sum over all possible pairs i and j. f_{ij} is the Mayer-f function

$$f_{ij}(\underline{r}) = e^{-\beta u_{ij}(\underline{r})} - 1 \qquad \text{Eq. 2.3.2}$$

where $u_{ij}(\underline{r})$ is the interaction energy between particles. For homogenous fluids, the densities will not be a function of position. It can then be noted that the pairwise interactions for hard sphere mixtures are defined purely by geometric constraints between two spheres with radiuses R_i and R_j.

$$u_{ij}(r) = \begin{cases} \infty & r < R_i + R_j \\ 0 & r \geq R_i + R_j \end{cases} \qquad \text{Eq. 2.3.3}$$

Rosenfeld showed that it is possible to uniquely define the Mayer-f function for hard sphere interactions as a sum of three dimensional convolutions of 6 different weighting functions, $\omega^{(k)}$, for each component

$$-f_{ij}(\underline{r}) = \omega_i^{(3)} * \omega_j^{(0)} + \omega_j^{(3)} * \omega_i^{(0)} + \omega_i^{(1)} * \omega_j^{(2)} + \omega_j^{(1)} * \omega_i^{(2)} + \underline{\omega}_i^{(1)} * \underline{\omega}_i^{(2)} + \underline{\omega}_j^{(1)} * \underline{\omega}_i^{(2)} \quad \text{Eq. 2.3.4}$$

where $*$ is the three-dimensional convolution. These equations lead to weighted densities, $\eta_{(k)}$, equal to the convolution of the local density with the weighting functions.

$$\eta_{(k)}(\underline{r}) = \sum_{i=1}^{N} \int d\underline{r}' \rho_i(\underline{r}') \omega_i^{(k)}(\underline{r} - \underline{r}') \quad \text{Eq. 2.3.5}$$

$$\omega_i^{(3)}(\underline{r}) = \Theta(R_i - r) \quad \text{Eq. 2.3.6}$$

$$\omega_i^{(2)}(\underline{r}) = \delta(R_i - r) \quad \text{Eq. 2.3.7}$$

$$\omega_i^{(1)}(\underline{r}) = \frac{\omega_2^{(2)}(\underline{r})}{4\pi R_i} \quad \text{Eq. 2.3.8}$$

$$\omega_i^{(0)}(\underline{r}) = \frac{\omega_i^{(2)}(\underline{r})}{4\pi R_i^2} \quad \text{Eq. 2.3.9}$$

$$\underline{\omega}_i^{(2)}(\underline{r}) = \frac{\underline{r}}{r}\delta(R_i - r) \quad \text{Eq. 2.3.10}$$

$$\underline{\omega}_i^{(1)}(\underline{r}) = \frac{\underline{\omega}_i^{(2)}(\underline{r})}{4\pi R_i} \quad \text{Eq. 2.3.11}$$

where Θ is the Heaviside function and δ is the Dirac-delta function. There are four scalar weighting functions that integrate to the fundamental geometric measures of a sphere for a homogenous hard sphere fluid. Two vector weighting functions are non-zero only when there is an external field in the system. Thus in the homogenous fluid, these equations reduce to Scaled Particle Theory [59]. This leads to the thermodynamics of hard spheres constructed by Rosenfeld's fundamental measure theory to be governed by the Percus-Yevick compressibility equation

$$\frac{\beta P}{\rho} = \frac{1 + \eta + \eta^2}{1 - \eta^3} \quad \text{Eq. 2.3.12}$$

where η is the packing fraction of the spheres. It can also be seen that the bulk value of $\eta_{(3)}$ is simply equal η. Rosenfeld then makes an assumption on the form of the excess energy such that

$$\beta \mathcal{F}_{ex}[\{\rho_i\}] = \int d\underline{r} \Phi[\{\eta_{(k)}(\underline{r})\}] \quad \text{Eq. 2.3.13}$$

where Φ is a reduced free energy density and only a function of the weighted density function. This allows the excess energies to be determined purely by the fluid density and diameters. Using

dimensional analysis on Φ, Rosenfeld derived a relationship with five unknown functions and the weighted densities.

$$\Phi = f_1(\eta_{(3)})\eta_{(0)} + f_2(\eta_{(3)})\eta_{(1)}\eta_{(2)} + f_3(\eta_{(3)})\underline{\eta}_{(1)} \cdot \underline{\eta}_{(2)} + f_4(\eta_{(3)})\eta_{(2)}^2 + f_5(\eta_{(3)})\eta_{(2)}\underline{\eta}_{(2)} \cdot \underline{\eta}_{(3)} \quad \text{Eq. 2.3.14}$$

Rosenfeld then used Scaled Particle Theory (SPT) to tie the hard sphere interactions to thermodynamics to find the unknown functionals.

$$\lim_{R_i \to \infty} \frac{\mu_{ex,i}}{V_i} = P \quad \text{Eq. 2.3.15}$$

In SPT, the excess chemical potential is approximated by the amount of work needed to add an additional hard sphere to the mixture as seen in Eq. 2.3.15. It is important to note that this equation produces the low density limit for hard spheres exactly; however, it is an approximation for higher densities as seen in liquids. This equation of state leads to a relationship between the excess chemical potential and the reduced free energy density of the system.

$$\beta\mu_{ex,i} = \frac{\partial\Phi}{\partial\rho_i} = \sum_k \frac{\partial\Phi}{\partial\eta_{(k)}}\frac{\partial\eta_{(k)}}{\partial\rho_i} \quad \text{Eq. 2.3.16}$$

Using dimensional analysis and ensuring that the equations correctly deconvolute into the Mayer-f function, the reduced free energy density terms can then be solved.

$$\Phi = -\eta_{(0)}\ln(1-\eta_{(3)}) + \frac{\eta_{(1)}\eta_{(2)}}{1-\eta_{(3)}} + \frac{1}{24\pi}\frac{\eta_{(2)}^3}{(1-\eta_{(3)})^2} - \frac{\underline{\eta}_{(1)} \cdot \underline{\eta}_{(2)}}{1-\eta_{(3)}} - \frac{1}{8\pi}\frac{\eta_{(2)}\left(\underline{\eta}_{(1)} \cdot \underline{\eta}_{(2)}\right)}{(1-\eta_{(3)})^2} \quad \text{Eq. 2.3.17}$$

where the first three terms correspond to the scalar weighting functions and the last two terms correspond to the vector weighting functions. The details on how to derive the one-body direct correlation term for the Rosenfeld functional is shown in Appendix A.

To validate the code and display the performance of the Rosenfeld hard sphere functionals, an example calculation is done for binary hard spheres adjacent to a hard wall. The details of the numerical methods are more thoroughly outlined in Chapter 3.

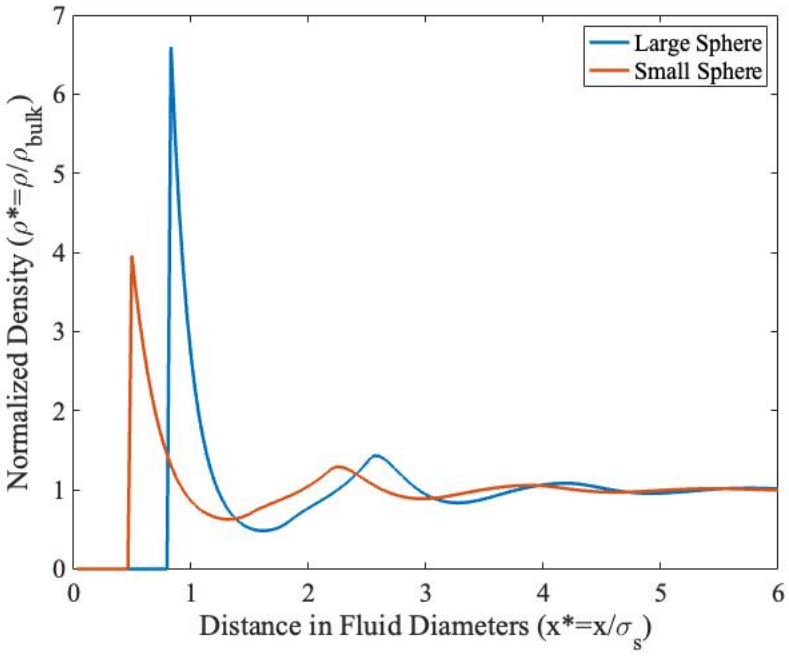

Figure 2-1: Normalized density distributions of a binary hard sphere mixture close to a hard wall. The bulk values for each curve are normalized to their respective values. The chosen parameters were taken from [1].

The large sphere diameter to small sphere diameter ratio is set at $\frac{5}{3}$. The small sphere packing fraction is set at 0.0607 while the large sphere packing fraction is set at 0.3105. These values are chosen to replicate the simulation study by [1]. It can be seen that there is good agreement in the predicted density profiles, validating the implemented hard sphere mixture code.

The locations of the first peak is at $x^* = 0.5$ due to the distance of closest approach for the small sphere and similarly for the large sphere at $x^* = \frac{5}{6}$. The second peak of the small sphere is at about $x^* = 2.25$ rather than at about $x^* = 1.5$. This shift in peaks can be understood by the interactions in repulsion between the large spheres and small spheres. The high density of the large sphere from its first layer causes the smaller spheres to be pushed away further from the wall in its second peak. This simple simulation shows the effects of volume exclusion can have from a wall potential onto their density distributions.

2.4 Dipolar Poisson-Boltzmann Theory

Despite the successes of other theories in predicting solvent electrostatic interactions, they lose the simple interpretability of Poisson-Boltzmann style theories. A dipolar Poisson-Boltzmann theory has been derived using many-body mean field theory to analyze the construction of a point dipole and point charge distributions in the vicinity of charged interfaces [61]. The same equation can actually be derived using the formalism involved in density functional theory and this derivation will be briefly illustrated [62].

The dipolar Poisson-Boltzmann equation was derived similarly to the Poisson-Boltzmann equation, where the divergence of the electric field is equal to the charge accumulation using mean field coulombic interactions. Unlike the Poisson-Boltzmann equation, the dipolar Poisson-Boltzmann equation was derived by considering the charge density distribution, ρ_c, of free dipoles and free charges in an electric potential

$$\rho_c(\underline{r}) = -\sum_{D=1}^{M} \int d\underline{p}_D \left[\underline{p}_D \cdot \underline{\nabla}\hat{\rho}_D(\underline{r}, \underline{n})\right] + \sum_{I=1}^{N} z_I e \rho_I(\underline{r}) \qquad \text{Eq. 2.4.1}$$

where M is the total number of dipole types, N is the total number of ion types, D is the dipole index, I is the ion index, $\hat{\rho}_D$ is the one particle distribution of dipoles, and $\underline{n}$ is the orientational vector of the dipole. It can be recognized that the total distribution of dipoles within an electric field is simply equal to the polarization density $\underline{P}$. Following the derivation in Appendix B and assuming that there is only one type of dipolar species in the domain, the modified dipolar Poisson-Boltzmann equation is found.

$$\nabla \cdot \left[\left(1 + \frac{\rho_D p_0 \mathrm{L}(\beta p_0 |\nabla\phi|)}{\epsilon_0 |\nabla\phi|}\right) \nabla\phi(\underline{r})\right] = -\frac{1}{\epsilon_0} \sum_{I=1}^{N} z_I e \rho_I(\underline{r}) \qquad \text{Eq. 2.4.2}$$

It can be seen that this leads to an equation similar to the Poisson-Boltzmann equation with the key difference being that the local relative permittivity is no longer a constant. Instead, it is a function of the temperature, dipolar properties, density, and local electric field.

$$\epsilon_r(\rho_D, \nabla\phi, \beta) = 1 + \frac{\rho_D p_0 L(\beta p_0 |\nabla\phi|)}{\epsilon_0 |\nabla\phi|} \qquad \text{Eq. 2.4.3}$$

The dipolar density, ρ_D, is kept as a general term so that the equation can be coupled to other free energy functionals from the c-DFT solver. This is in contrast to the original dipolar Poisson-

Boltzmann equations where the dipole density is analytically solved when the only excess free energy considered is electrostatic [62].

$$\epsilon_r(\rho_D, \nabla\phi, \beta) = \begin{cases} 1, & |\nabla\phi| \to \infty \\ 1 + \dfrac{\beta\rho_D p_0^2}{3\epsilon_0}, & |\nabla\phi| \to 0 \end{cases} \quad \text{Eq. 2.4.4}$$

The behavior of the local relative permittivity can be understood by taking the limits of the electric field. When the electric field approaches infinity, then the Langevin function will saturate, leading the predicted relative permittivity to be 1. This can be understood as the dipoles being so strongly aligned with the external electric field that it does not effectively screen the electric field. When the electric field approaches 0, then the relative permittivity will reduce to the bulk value predicted by Eq. 2.4.4. It can be seen that this term is identical to the first order term estimated in the Debye equation.

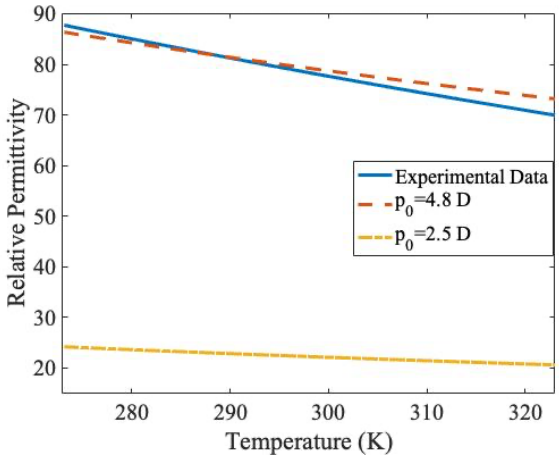

Figure 2-2: The relative permittivity of water versus temperature for experimental values [2] and the predicted bulk value using Langevin styled equation in the dipolar Poisson-Boltzmann equation with different dipole moments.

It is important to note here some key assumptions made in the dipolar Poisson-Boltzmann equation. The largest assumption made in this equation is that all electrostatic interactions are in the mean field. As seen by Eq. 2.1.7, this means that correlations are ignored. This will cause the predicted bulk relative permittivity to be under-predicted for water as covered in Chapter 1. At the cost of accuracy in describing polar solvent interactions, this method gives a simple and easy to

interpret result. This allows it to be a good first step in determining double layer adsorption processes.

The excess free energies for inhomogeneous charged species can then be calculated using basic electrostatic principles.

$$\mathcal{F}_{ex,I} = \frac{1}{2}\int q_I e \rho_I(\underline{r})\phi(\underline{r})d\underline{r} \qquad \text{Eq. 2.4.5}$$

$$\mathcal{F}_{ex,D} = \frac{1}{2}\int \rho_D(\underline{r}) < \underline{p}_D(\underline{r}) \cdot \underline{\nabla}\phi(\underline{r}) > d\underline{r} \qquad \text{Eq. 2.4.6}$$

The excess free energy of the dipole at a position is equal to the expected value of the dot product between the dipole vector and the electric field gradient at that point. The average angle can be easily extracted using statistical mechanics and follows Eq. 1.2.5.

As a result, the density distribution functions can be calculated for each species using Eq. 2.1.5 and plugging in the one-body direct correlation terms for hard sphere and electrostatic interactions.

$$\rho_I(\underline{r}) = \rho_{I,bulk}\exp\left(-\beta V_{ext,i}(\underline{r}) - \beta\left(\frac{\delta\mathcal{F}_{ex,HS}}{\delta\rho_I} + \frac{\delta\mathcal{F}_{ex,I}}{\delta\rho_I}\right) + \beta\mu_{ex}\right) \qquad \text{Eq. 2.4.7}$$

$$\rho_D(\underline{r}) = \rho_{D,bulk}\exp\left(-\beta V_{ext,i}(\underline{r}) - \beta\left(\frac{\delta\mathcal{F}_{ex,HS}}{\delta\rho_D} + \frac{\delta\mathcal{F}_{ex,D}}{\delta\rho_D}\right) + \beta\mu_{ex}\right) \qquad \text{Eq. 2.4.8}$$

where $\frac{\delta\mathcal{F}_{ex,HS}}{\delta\rho_I}$ is the one-body direct correlation equation from fundamental measure theory. Now with all of the theories outlined on how to calculate the thermodynamics for the electrolyte model, the numerical methods on how these equations are implemented will be discussed in Chapter 4.

Chapter 3: Numerical Implementation

The code has been implemented to solve the density distribution of adsorbed fluids in one-dimensional space. The initial code was written in Matlab by Dr. Jiawei Zhou for single component van der Waals fluids. Additional capabilities were added in this work to compute properties of mixtures and electrostatic interactions. To solve for the fluid density distribution, the Matlab code uses a picard iteration scheme until the overall energy is minimized. In addition to the picard iteration scheme, a finite volume method is used to calculate the electrostatic potential within the domain. The dipolar effects in the electrostatic potential leads to a set of highly nonlinear equations. This chapter is devoted to discussing the numerical methods involved.

3.1 Discretization, Picard Iteration, and Error Evaluation

The one-dimensional domain is split into N evenly spaced grid points between two slit walls. The boundary conditions of the domain is set by the wall-fluid potential exerted by the slit. This leads to a one-dimensional vector that stores the density of each fluid component inside of the studied domain. For the purposes of this study, the grid spacing is always set to 0.02σ where σ is the diameter of the hard sphere.

The density distribution of each component inside of the domain is solved using a Picard iteration scheme on Eq. 2.4.7 and Eq. 2.4.8 for each component. Ideally, an initial guess for the density vectors are given that is close to the equilibrium values to improve the speed of calculation; however, it may not always be clear what would be an appropriate guess value for different case studies. All initial guess are set at $\frac{\rho_i(\boldsymbol{r})}{\rho_{i,bulk}} = 1$ to standardize this process. The mixing factor is utilized to improve the stability of the iterations, although at a cost of more computation time if the mixing factor is small. For example in Rosenfeld's reduced free energy density term in Eq. 2.2.17, $\eta_{(3)}$ cannot be larger than 1 or else the natural logarithmic equation will diverge. This can be understood physically as the packing fraction of a sphere mixture cannot exceed 1. If too large a step is taken in the Picard iteration, then the new density vectors can easily lead to a η_3 value greater than 1. The mixing factor is set to a maximum value of 0.05.

The density is considered to be converged when the change in the density vectors are sufficiently small between iterations. This error, E, is evaluated using a ratio in the 2-norm of the change in density to the 2-norm of the total density.

$$\mathrm{E} = \frac{\left\| \underline{\rho}^{j+1} - \underline{\rho}^{j} \right\|_2}{\left\| \underline{\rho}^{j} \right\|_2} \qquad \text{Eq. 3.1.1}$$

$$\left\| \underline{x} \right\|_2 = \sqrt{\sum_{i=0} |x_i|^2} \qquad \text{Eq. 3.1.2}$$

where the superscript j corresponds to the current iteration. The subscript i in Eq. 3.1.2 corresponds to the elements in the vector x. The error tolerance is set to 1e-4 for the purposes of this study.

3.2 Non-Electrostatic Free Energy Calculations

The non-electrostatic free energies are calculated using simple algebra of their excess energy functionals. Each of the weighting functions in Eq. 2.3.6 to 2.3.11 are mapped out onto sparse square matrices. The characteristic size of the sparse matrix is equal to the number of grid points within the studied domain. Each row corresponds to the weighting function of a single hard sphere mapped out onto each grid point starting from the left-most grid point. This leads to a band matrix with the number of non-zero diagonals equal to the number of grid points that can fit inside the sphere's diameter.

The matrices are then multiplied by the density vectors of each component and summed together to give the weighted densities in Eq. 2.3.5. This procedure is done for each component to calculate the total weighted densities of the mixture. Afterwards simple algebra is used based on Appendix A to calculate the one-body direct correlation terms for the hard sphere repulsions.

3.3 Electrostatic Free Energy Calculations

Solving the electrostatic interactions in the system is an involved calculation due to the high non-linearity in the dipolar Poisson-Boltzmann equation. Using a finite volume method, the

dipolar Poisson-Boltzmann equation can be discretized using staggered grids based on the density vector discretizations to self-consistently solve the electrostatic potential field [63]. The electrostatic potential field is then iterated using multivariate Newton's method until a converged equation is found.

3.3.1 Discretization Using Finite Volume Method

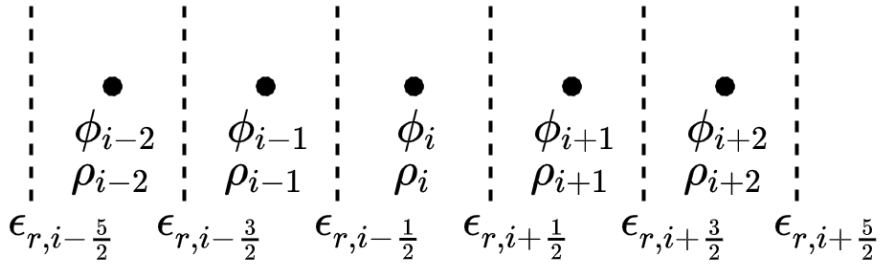

Figure 3-1: Discretization of domain using staggered grids for the dipolar Poisson-Boltzmann solver.

The dipolar Poisson-Boltzmann equation is a non-linear second order partial differential equation in space. Eq. 2.4.2 states that the divergence of the electric field through a dielectric material must equal to the charge density. This equation can be discretized using the divergence theorem

$$\int_V \left(\underline{\nabla} \cdot \underline{F}\right) dV = \int_{\partial V} \underline{F} \cdot d\underline{A} \qquad \text{Eq. 3.3.1}$$

where the integral of the divergence of a vector $\underline{F}$ over a finite volume must equal to the surface integral of $\underline{F}$. If the dipolar Poisson-Boltzmann equation is treated in one-dimension, then the surface integral can be written as

$$\int_{\partial V} \nabla \cdot [\epsilon_r(x) \nabla \phi(x)] d\underline{A} = A_{yz} \epsilon_{r,i-\frac{1}{2}} \frac{\phi_i - \phi_{i-1}}{dx} + A_{yz} \epsilon_{r,i+\frac{1}{2}} \frac{\phi_i - \phi_{i+1}}{dx} \qquad \text{Eq. 3.3.2}$$

where A_{yz} is the cross-sectional area perpendicular to the x-direction, the relative permittivity values are sampled at half-staggered grid point with notation $i \pm \frac{1}{2}$, and electric potentials sampled at grid point i as seen in Figure 3-1. The electric field, $\frac{d\phi}{dx}$, is linearly approximated between the

adjacent grid points. The relative permittivity values are sampled at half-staggered grid points to better approximate the electric flux passing through the surface of the discretized domain.

The local relative permittivity is a function of both dipole density and electric fields. When solving for the local relative permittivity, it was found that using only single grid point densities led to predicted relative permittivity values too large. This is because the relative permittivity function has a linear dependence on the dipolar density and the characteristic peak heights from the Rosenfeld functional tend to be large. As a result, a weighted average density in the spirit of hard spheres were used when calculating the local relative permittivity similar to what was used in [57].

$$\widetilde{\rho_D}(x) = \frac{\int_{x-\frac{\sigma}{2}}^{x+\frac{\sigma}{2}} dx' \rho_D(x) \Theta\left(\frac{\sigma}{2} - x\right)}{\int_{x-\frac{\sigma}{2}}^{x+\frac{\sigma}{2}} dx' \Theta\left(\frac{\sigma}{2} - x\right)} \qquad \text{Eq. 3.3.3}$$

This weighted average effectively smooths out very large peaks in the density distributions using a weighting scheme similar to how mass is distributed in a sphere along the x-axis. Without this averaging scheme, the relative permittivity becomes so large that the electric field is essentially 0 outside of the first layer of adsorbed dipoles.

The integral of the charge density of the right hand side of the dipolar Poisson-Boltzmann equation would simply equal to the total charge in the finite volume.

$$\int_V -\frac{1}{\epsilon_0} C z_I \rho_I(\underline{r}) dV = -\frac{A_{yz}}{\epsilon_0} C z_I \rho_I(x) dx \qquad \text{Eq. 3.3.4}$$

The equations were then non-dimensionalized to improve the stability of the numerics and allow a consistent error tolerance be used between different cases.

$$\phi^* = \frac{\phi}{\psi} \qquad \text{Eq. 3.3.5}$$

$$dx^* = \frac{dx}{\sigma} \qquad \text{Eq. 3.3.6}$$

$$\epsilon_{r,i-\frac{1}{2}}(\phi_i^* - \phi_{i-1}^*) + \epsilon_{r,i+\frac{1}{2}}(\phi_i^* - \phi_{i+1}^*) + \frac{C\sigma^2}{\psi\epsilon_0} \sum_{I=1}^{N} z_I \rho_{I,i} dx^{*^2} = 0 \qquad \text{Eq. 3.3.7}$$

ψ is the characteristic electrostatic potential and σ is the fluid diameter. This choice of re-arrangement allows all values to be on orders of magnitude close to unity. If the relative permittivity was treated as constant, similar to what is used in Poisson-Boltzmann equation, then

Eq. 3.3.7 would form a system of linear equations; however, the dependence of the relative permittivity on the gradient of ϕ lead to non-linear coefficients. Eq. 3.3.7 for all grid points can be written as a vector $\underline{F}$

$$\underline{F}\left(\underline{\phi}^*\right) = \underline{\underline{A}}\,\underline{\phi}^* + \underline{B} + \underline{C} \qquad \text{Eq. 3.3.8}$$

where $\underline{\underline{A}}$ is a tridiagonal matrix with the relative permittivity coefficients, $\underline{B}$ is a vector corresponding to the total charge in each finite volume, $\underline{C}$ is a vector that includes the boundary conditions to the dipolar Poisson-Boltzmann equation, and $\underline{\phi}^*$ is a column vector corresponding to the electrostatic potential on grid points i. $\underline{F}$ can be thought of as the error in the electrostatic potential because it should be equal to 0 for the converged electrostatic potential field. Two Dirichlet boundary conditions will be used for the electrostatic potential for the chosen studies.

3.3.2 Newton's Method and Solving for Electrostatic Potential

Eq. 3.3.8 can then be solved iteratively using multivariate Newton's method

$$\underline{\underline{F'}}\left(\underline{\phi}^*\right) = \frac{\delta \underline{F}\left(\underline{\phi}^*\right)}{\delta \underline{\phi}^*} = \underline{\underline{A}} + \frac{\delta A}{\delta \phi}\underline{\phi}^* + \frac{\delta \underline{C}}{\delta \phi} \qquad \text{Eq. 3.3.9}$$

$$\underline{\phi}^{*(guess)} = \underline{\phi}^{*(k)} - \underline{\underline{F'}}\left(\underline{\phi}^{*(k)}\right)^{-1}\underline{F}\left(\underline{\phi}^{*(k)}\right) \qquad \text{Eq. 3.3.10}$$

where k denotes the iteration and $\underline{\underline{F'}}$ is the Jacobian of the function. The details of all the terms in the Jacobian can be found in more detail in Appendix C. $\underline{\phi}^{*(guess)}$ is the new electrostatic potential field if the full perturbation step is taken. To improve the stability of the dipolar Poisson-Boltzmann a mixing function is applied for calculating the new potential field. This ensures that the perturbation vector calculated from the Jacobian won't overshoot the solution

$$\underline{\phi}^{*(k+1)} = \lambda_{DPB}\underline{\phi}^{*(guess)} + (1 - \lambda_{DPB})\underline{\phi}^{*(k)} \qquad \text{Eq. 3.3.11}$$

where λ_{DPB} is the mixing parameter between 0 and 1. For the purposes of this study, λ_{DPB} is typically set to 0.1. The most computationally intensive step in this algorithm is in fact calculating the inverse Jacobian and iterating through multivariate Newton's method.

It can be noticed that the Langevin function can lead to issues numerically when the electric field is close to 0 due to the hyperbolic cotangent function and its denominator approaching 0. As

seen in Eq. 2.4.4, the relative permittivity should reduce to bulk value when the electric field is 0. This allows us to accurately estimate the Langevin function using a Taylor expansion about 0. It was found through testing that unstable fluctuations typically occur when $Z = \beta \left|\frac{d\phi}{dx}\right| p_D$ is less than 1e-4.

$$\epsilon_r = \begin{cases} 1 + \dfrac{\rho_D p_D \, \mathrm{L}(Z)}{\epsilon_0 |\nabla \phi|}, & Z > 10^{-4} \\ 1 + \dfrac{\rho_D p_D}{\epsilon_0 |\nabla \phi|} \left[\dfrac{1}{3} Z - \dfrac{1}{45} Z^3 + \dfrac{2}{945} Z^5 - \dfrac{1}{4724} Z^7\right], & Z \leq 10^{-4} \end{cases} \qquad \text{Eq. 3.3.12}$$

The derivatives of the relative permittivity with respect to the electrostatic potential is derived using the same criteria for Z and can be found in the Appendix C.

The error of each iteration, E_{DPB}, is calculated using the root-mean-square error of the vector $\underline{F}$

$$\mathrm{E}_{DPB} = \sqrt{\frac{\sum_{i=1}^{N} F_i^2}{N}} \qquad \text{Eq. 3.3.13}$$

where N is the size of the vector and i is the element index. The error tolerance for the dipolar Poisson-Boltzmann solver is set at 1e-7.

Chapter 4: Three Component Electrolyte with Dipolar Solvent

The system of interest to study is the primitive three component electrolyte in nanopore slits. Many electrochemical devices use nanoporous electrodes to improve capacitor performance. In nanopore slits, the small distance between adjacent walls lead to double layers overlapping with one another. Furthermore, the comparable size between the slit distance and the atomic species leads to important steric effects that will impact adsorption properties. These effects are not well accounted for classical macroscopic theories; however, they can be probed using the proposed c-DFT formalism.

4.1 Electrostatic Free Energy Calculations

A number of simplifications were made to reduce the degrees of freedom in this study to understand the dipolar Poisson-Boltzmann's fundamental behaviors in classical density functional theory. As a result, the total excess free energy is the sum of hard sphere repulsion and electrostatic interactions similar to the primitive 3 component electrolyte.

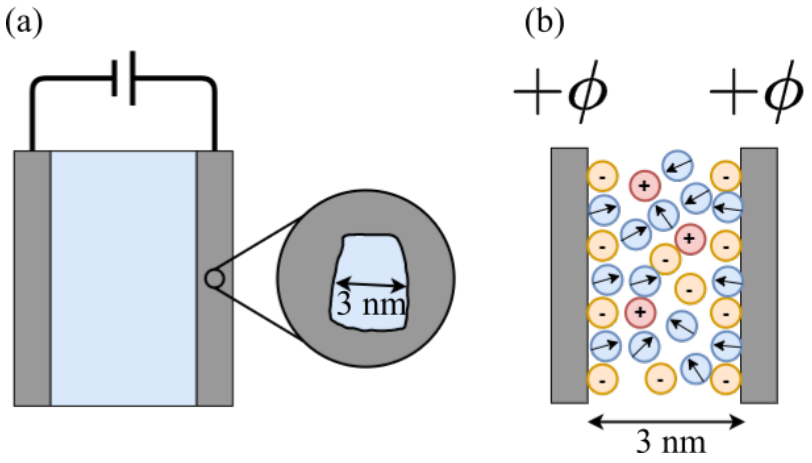

Figure 4-1: Studied domain in the present study. (a) shows the macroscopic system of a capacitor system with nanoporous electrodes. (b) shows idealized slit pore geometry used to approximate the nanopores.

The studied system is a one-dimensional slab geometry with symmetric boundary conditions as shown in Figure 4-1. Symmetric boundary conditions can correspond to nanopores found in electrodes set to constant surface potentials. The boundary conditions used in this study are a hard wall with a constant electric potential. The electric potential is varied from 0.05 V to 0.3 V.

$$V_{Hard-wall} = \begin{cases} \infty, & x < R \\ 0, & otherwise \end{cases} \quad \text{Eq. 4.1.1}$$

All species are set to have the same hard sphere diameter at 3 Angstroms, which is close to the diameter of water, anions and some large cations. The bulk density of the liquid was set at water's number density in 298 K and the density of electrolytes is set at 0.1 M. It is assumed that water's density changes due to temperature and ions are negligible.

Table 4.1: Parameters used for the current study in each of the different cases for electrolyte structure in nanoslit geometry.

Parameters	Base Case	Wall Potential	Dipole Moment	Temperature	Length
$\phi_{wall}\ (V)$	0.2	0.1, 0.2, 0.3	0.2	0.2	0.2
$p_0\ (D)$	4.8	4.8	2.5, 4.8	4.8	4.8
$T\ (K)$	298	298	298	283, 298, 313	298
$x_{max}(\sigma)$	10	10	10	10	5, 7, 10

4.2 Wall Potential Effects

The first case that will be studied is the effects of different surface wall potentials on the structure and potential field within the nanoslit geometry. The choice of wall potential is expected to play one of the largest roles in determining how ions and solvent structures itself due to its large influence on the electrostatic potential field.

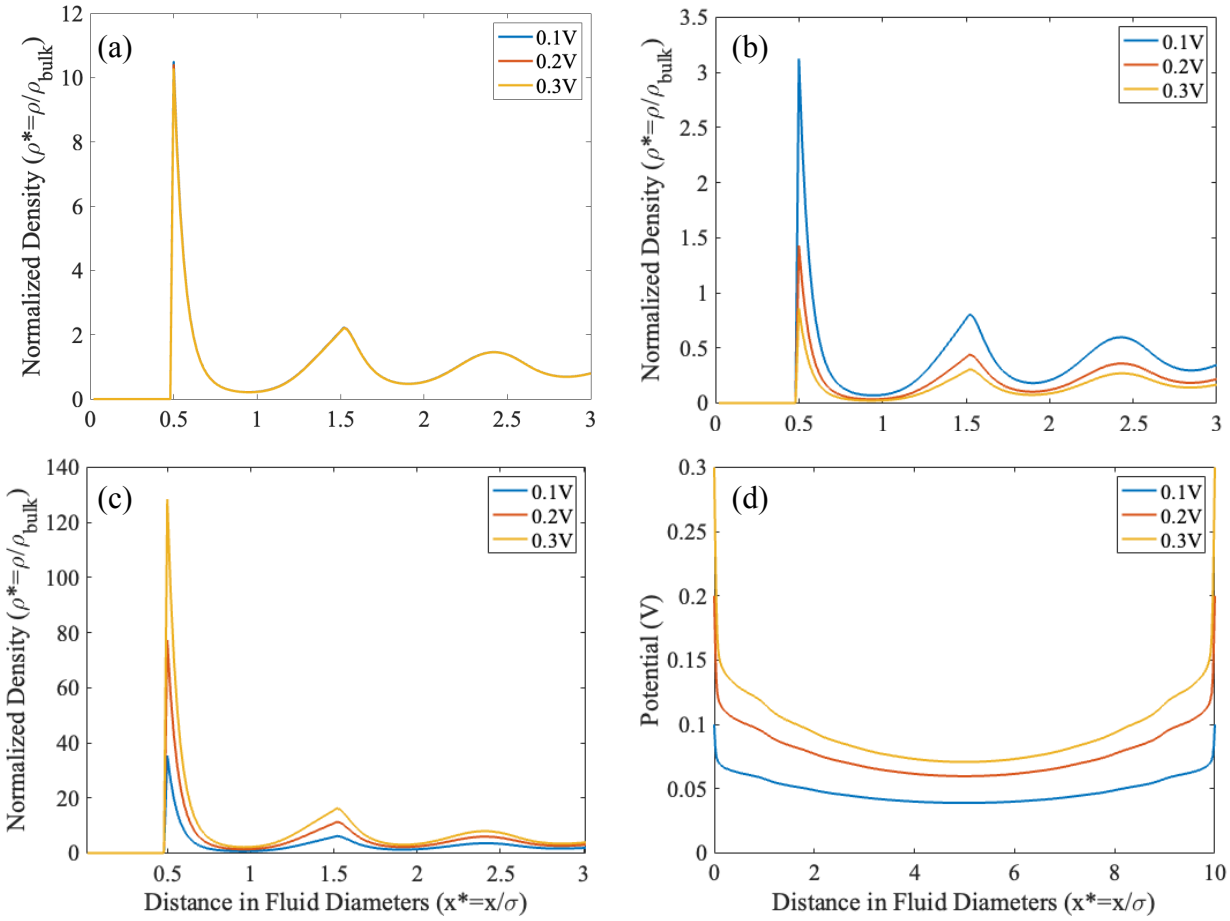

Figure 4-2: The density profiles of (a) solvent, (b) cations, and (c) anions for different surface potentials as a function of distance from the capacitor wall. Each curve is normalized to their respective bulk densities. (d) shows the calculated potential curve in the full domain.

The first set of data to be analyzed is the density distributions of each species and the resulting electrostatic potential field within the domain geometry. It can be seen that the largest effects on the density profiles is for the ionic species. In Figure 4-2(a), the first peak for the dipolar solvent decreases slightly with increasing electrostatic potential. This is despite the electric field increasing, which should promote dipolar adsorption. The cation adsorption in the first peak decreases by about a factor of 3 and the anionic adsorption in the first peak increases by about a factor of 3 with increasing surface potential. From this, we can now understand why the polar solvent's density decreases close to the capacitor wall. Due to the extremely dense first layer of adsorbed anions from strong electrostatic interactions, the hard sphere repulsion also increases

significantly. This leads to the adsorption of the dipolar solvent to overall decrease with increasing electrostatic wall potential, as will be seen in Figure 4-5(a).

It can also be seen that the electrostatic potential curves displays some interesting behaviors. The electrostatic drop in the regions close to the wall is almost linear until the first layer of adsorbed species. This is similar in prediction to what is found in the Stern model with the inner Helmholtz layer. The electrostatic drop in this first linear region also contributes significantly to the potential drop from the slit wall to the midplane region. Also very interestingly, the midplane potential does not reach 0 V as what is commonly assumed in macroscopic models. This is because the overlapping double layers in the nanoconfined slit leads to a significant charge density to exist in the center. It can be seen that the midplane potential tends to decrease with decreasing wall potential. The midplane potential changes also does not seem to behave linearly with the wall potential. The difference in the midplane potential from 0.2 V to 0.1 V is almost double that of 0.3 V to 0.2 V.

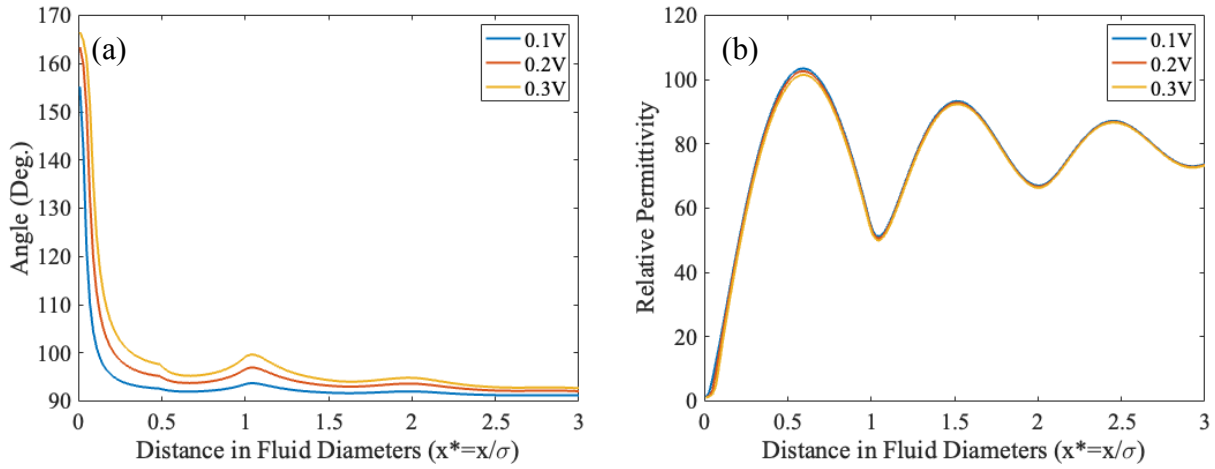

Figure 4-3: Properties of polar solvent due to the surface potential with (a) showing the dipole's relative angle to the electric field and (b) the local relative permittivity.

Finally, the dielectric properties of the solvent will be analyzed to understand wall potential effects on solvent reorganization. In Figure 4-3(a), the relative angle the solvent forms with respect to the electric field is presented. It is important to note that the solvent density is 0 at distances lower than 0.5σ due to hard sphere repulsions with the wall. As a result, the current model suggests that the orientation of the dipolar solvent with respect to the electric field is only slightly perturbed.

At 0.5σ, the relative angle formed for the 0.3 V curve is about 100^{o}, which is only 10^{o} higher than free rotation. It can be seen that the degree of alignment increases with increasing wall potential due to the larger electric fields present. The relative orientation also does not monotonically decrease. Instead, it can be seen that the orientations have peaks that closely align to the density distributions. This change in alignment is likely due to the large negative charges accumulated from unsymmetric ionic adsorption. This will lead to large electric fields to form in their vicinities that will influence the dipole angles.

Finally, the local relative permittivity will be analyzed in the studied domain. It can be seen that in Figure 4-3(b), the relative permittivity is initially 1 and quickly rises to about 100 within 0.5σ. The relative permittivity in the mid-point of the first adsorbed dipole layer is also higher than bulk due to the large dipole density. With increasing wall potential, the predicted relative permittivity decreases slightly due to small dipolar alignment effects. The current model predicts that it is primarily the local solvent density that governs the local relative permittivity because the local electric field isn't large enough to cause significant reorientations of the polar solvent.

4.3 Dipole Moment Effects

The next set of parameters that will be analyzed is the effect of solvent dipolar moment on adsorption and predicted effects on structure. To study this, dipole moments of the solvent was decreased from the base case of 4.8 D to 2.5 D. 4.8 D was chosen to reproduce the bulk relative permittivity of water whereas 2.5 D is the approximate dipole moment of liquid water after self-polarization effects [64]. As mentioned in Chapter 2, using a dipole moment of 2.5 D will lead to significant underpredictions in the bulk relative permittivity due to negligence of dipolar-dipolar correlation effects. Regardless, this analysis will give a first understanding on how solvent properties can lead to changes in the double layer adsorption.

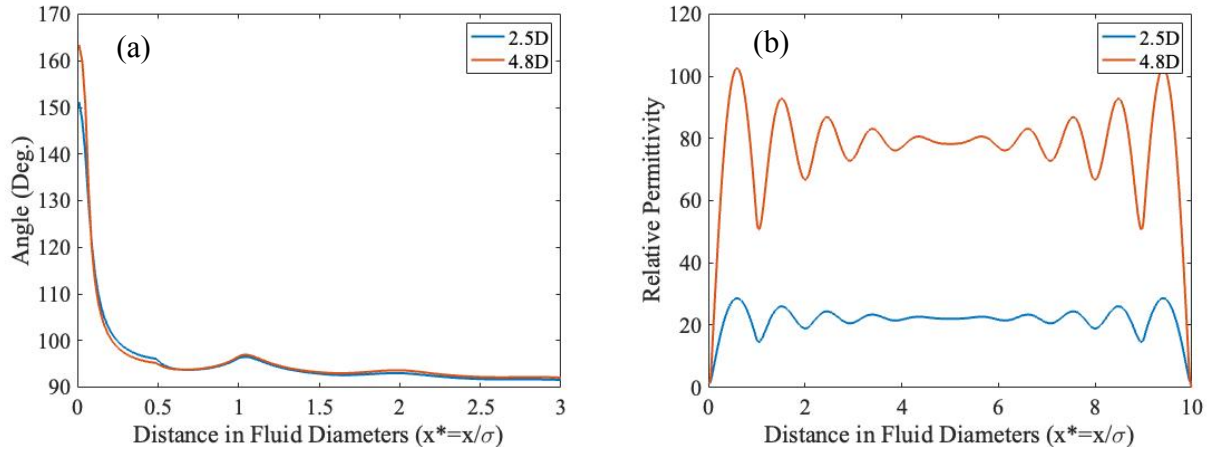

Figure 4-4: Properties of polar solvent due to the changing dipole moments with (a) showing the dipole's relative angle to the electric field and (b) showing the local relative permittivity .

The first result that can be analyzed is how solvent dielectric properties changes with dipole moment. The relative angle formed with respect to the electric field does not monotonically change as seen in Figure 4-4(a). Initially, the relative angle of the 2.5 D case is more aligned with the electric field in the inner Helmholtz layer. Afterwards, the 4.8 D case displays slightly higher alignment due to strong electrostatic coupling with the electric field. The local relative permittivity of the 2.5 D case is significantly lower than the 4.8 D case for all regions as shown in Figure 4-4(b). This is due to the bulk relative permittivity's squared dependence on the dipole moment in the dipolar Poisson-Boltzmann equation.

The next set of results that will be analyzed is the total excess adsorption predicted inside of the double slit capacitor. This curve was directly calculated from the density distribution curves using trapezoidal numerical integration.

$$A_{excess} = 100\% * \left(\frac{\int_0^{x_{max}} \rho^*(x) dx}{\int_0^{x_{max}} dx} - 1 \right) \qquad \text{Eq. 4.3.1}$$

where A_{excess} is the excess adsorption in percentage with respect to bulk and $\rho^*(x)$ is the normalized density distribution function. A negative value means that overall the component is depleted and a positive value means overall increased adsorption when compared to bulk. From this analysis, a number of interesting effects can be understood with how the choice of solvent can influence the total amount of charge a nanoporous capacitor can store at a given potential. It is

important to note that even with a 0 V wall potential there will be a net decrease in the excess adsorption due to hard wall repulsion effects from slit capacitor.

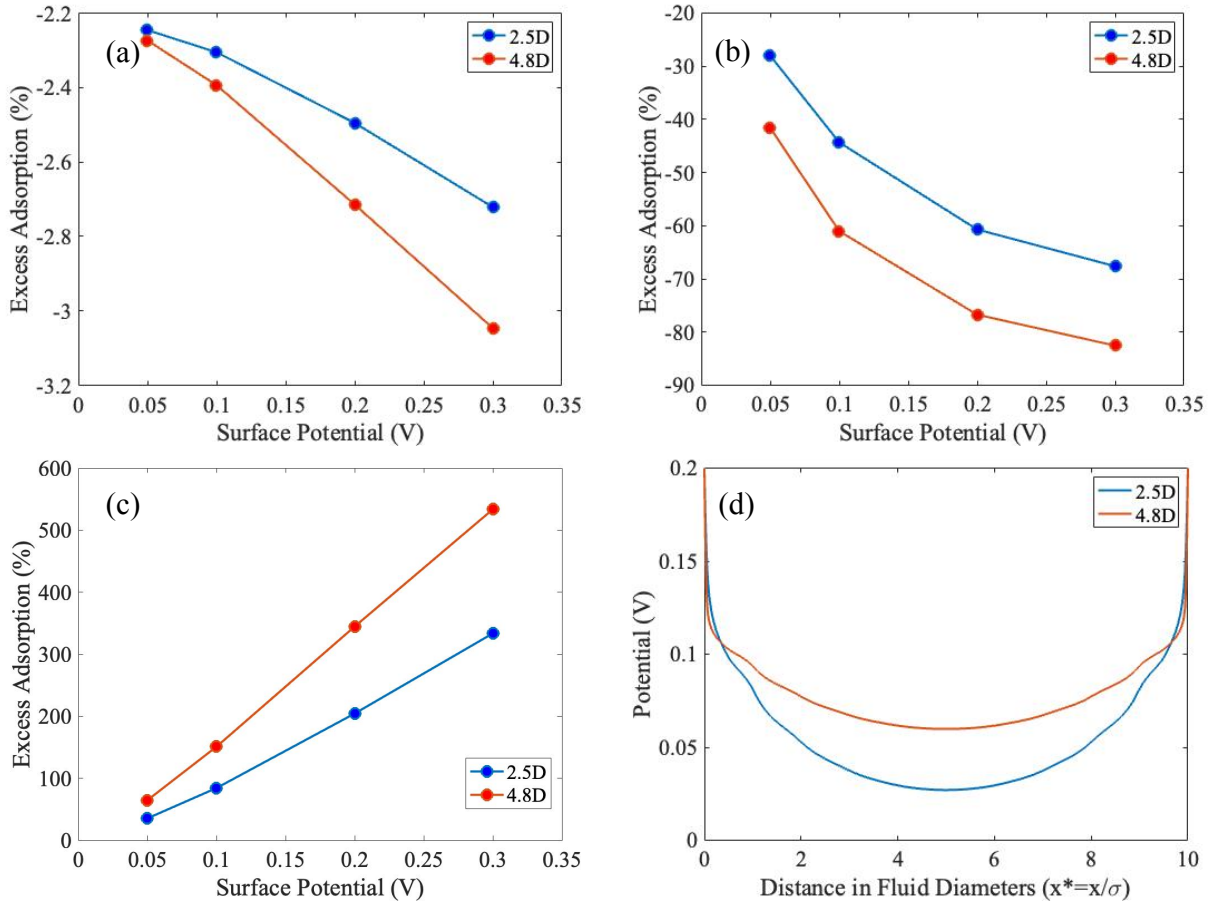

Figure 4-5: The excess adsorption of (a) solvent, (b) cations, and (c) anions as a function of surface potential and solvent dipole moment. (d) shows the predicted electrostatic potential as a function of distance for different dipole moments at a surface potential of 0.2 V.

It can be seen that the excess adsorption for the three different components follows different general patterns in the studied regions. For the polar solvent adsorption, it can be seen that the total excess adsorption decreases with increasing dipole moment. This is surprising result given that a larger dipole moment leads to strong electrostatic coupling with the electric field. Similarly, there is a net depletion in the cationic species that increases with the solvent dipole moment. The anionic excess adsorption in contrast increases with dipole moment. This results seems to contradict with classical macroscopic equations, where larger dielectric moments screens

the electric field more effectively. The reason for this odd behavior can be found in the predicted potential curves in Figure 4-5(d) for the 0.2 V boundary condition case. It can be seen in the inner Helmholtz plane close to the walls, the electric potential drops significantly faster for the 4.8 D solvent due to higher electrostatic screening. Afterwards, the electric field drops slower in the middle regions and leads to a midplane potential that is higher than the 2.5 D case. This increasing midplane region with respect to increasing dipole moment leads to higher anionic adsorption.

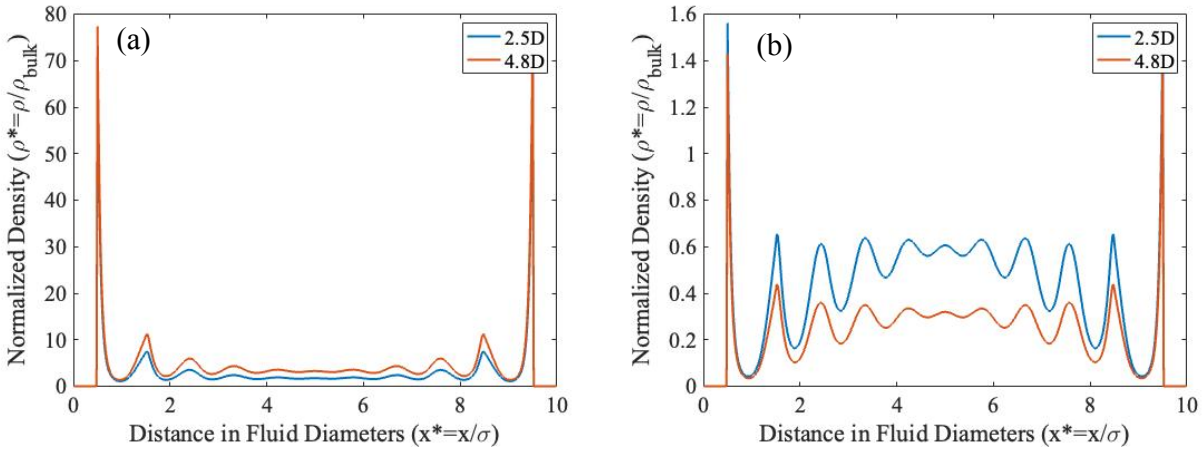

Figure 4-6: The density distributions of (a) anions and (b) cations in the studied domain at 0.2 V surface potential for different solvent dipolar moments.

The predicted potential curve also leads to some interesting behaviors in the density distributions of the ionic species. It can be seen in Figure 4-6(a) that the density distribution for anions in the 2.5 D case is lower than the 4.8 D throughout the entire domain and decays towards bulk value. For the cation distribution case, it can be seen that the amount of cations adsorbed in the midplane for the 2.5 D case is about double the amount in the 4.8 D case. This increased adsorption in center for cations is related to the decreased adsorption of anions and the higher midplane potentials.

4.4 Temperature Effects

Next we will analyze the predicted temperature effects on adsorption to understand the potential for charge storage in waste heat recovery applications. The studied temperature swing

was 30 K centered at room temperature, which is generally smaller than the working temperature for thermocapacitive devices. The smaller region was chosen to minimize the error in the predicted solvent dielectric properties as seen in Figure 2-2.

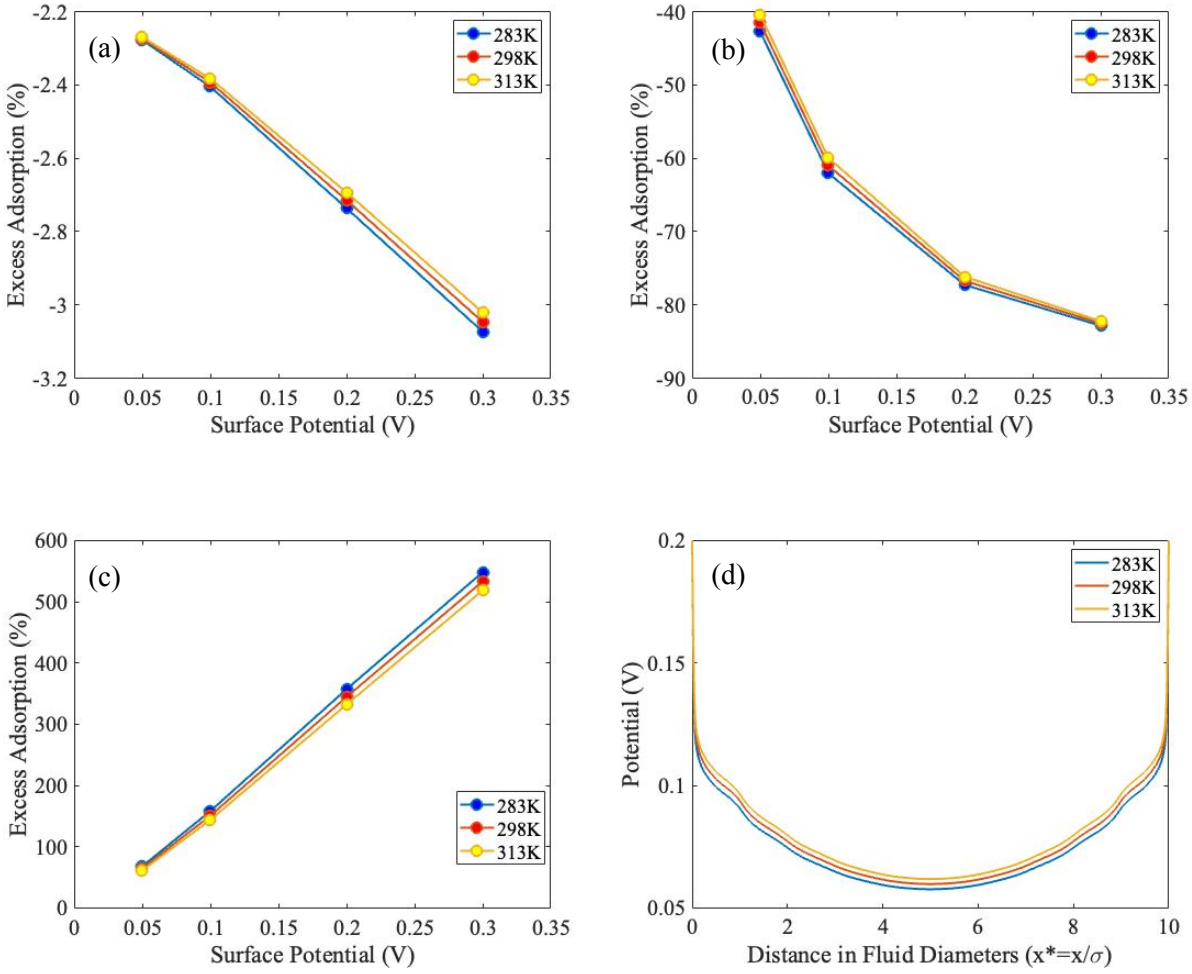

Figure 4-7: The excess adsorption of (a) solvent, (b) cations, and (c) anions as a function of surface potential and temperature. (d) shows the predicted electrostatic potential as a function of distance for different dipole moments at a surface potential of 0.2 V.

The first set of data analyzed is the excess adsorption and predicted potential curves while varying temperatures. It can be seen that the excess adsorption of both cations and solvent decreases with decreasing temperature as seen in Figure 4-7(a) and (b). This effect seems to increase at higher surface potentials for solvent as seen by the diverging curves in Figure 4-7(a). In contrast, Figure 4-7(c) shows that the excess adsorption of anions increases with decreasing

temperature. The curves also seem to diverge as well with increasing temperatures. This suggests that a larger charge adsorption swing with respect to temperature can be produced at higher capacitor surface potentials.

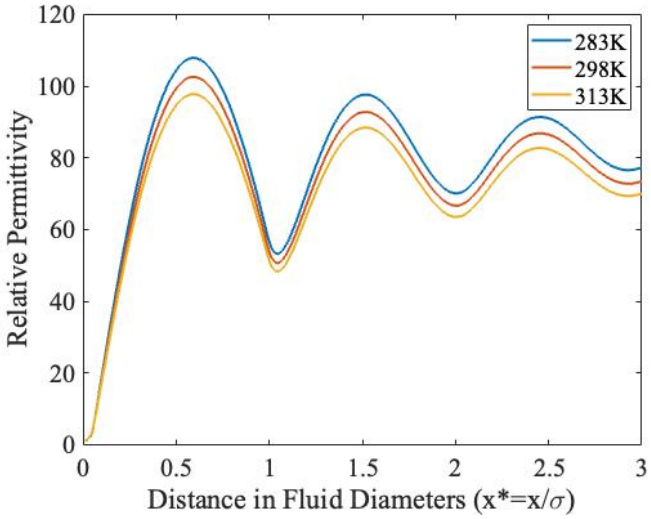

Figure 4-8: The local relative permittivity of solvent with respect to distance for different temperatures.

It can also be seen in Figure 4-(d) that the midplane potential tends to increase with increasing temperatures. This can be understood as the effects of overlapping double layers. The Debye length increases with the square root of temperature and square root of relative permittivity. Although the relative permittivity of the solvent decreases with temperature as seen in Figure 4-8, the temperature term in the Debye length dominates. This leads to an overall increased Debye length and subsequentially higher midplane potential due to double layer overlap.

4.5 Confinement Effects

The final set of results that will be analyzed is the effect of slit capacitor size on the total adsorbed charge. For Figures 4.6 and 4.7, the origin in the x-axis was reset to the center of the slit capacitor to make it easier to compare the density profiles. Confinement effects in this model can elucidate two competing effects. As the slit pore size gets smaller, the steric repulsion from the slit walls can play a dominating role and lead to overall less adsorption. The overlapping double layers

from the slit capacitor can also lead to coupling effects due to the higher surface potential in the midplane.

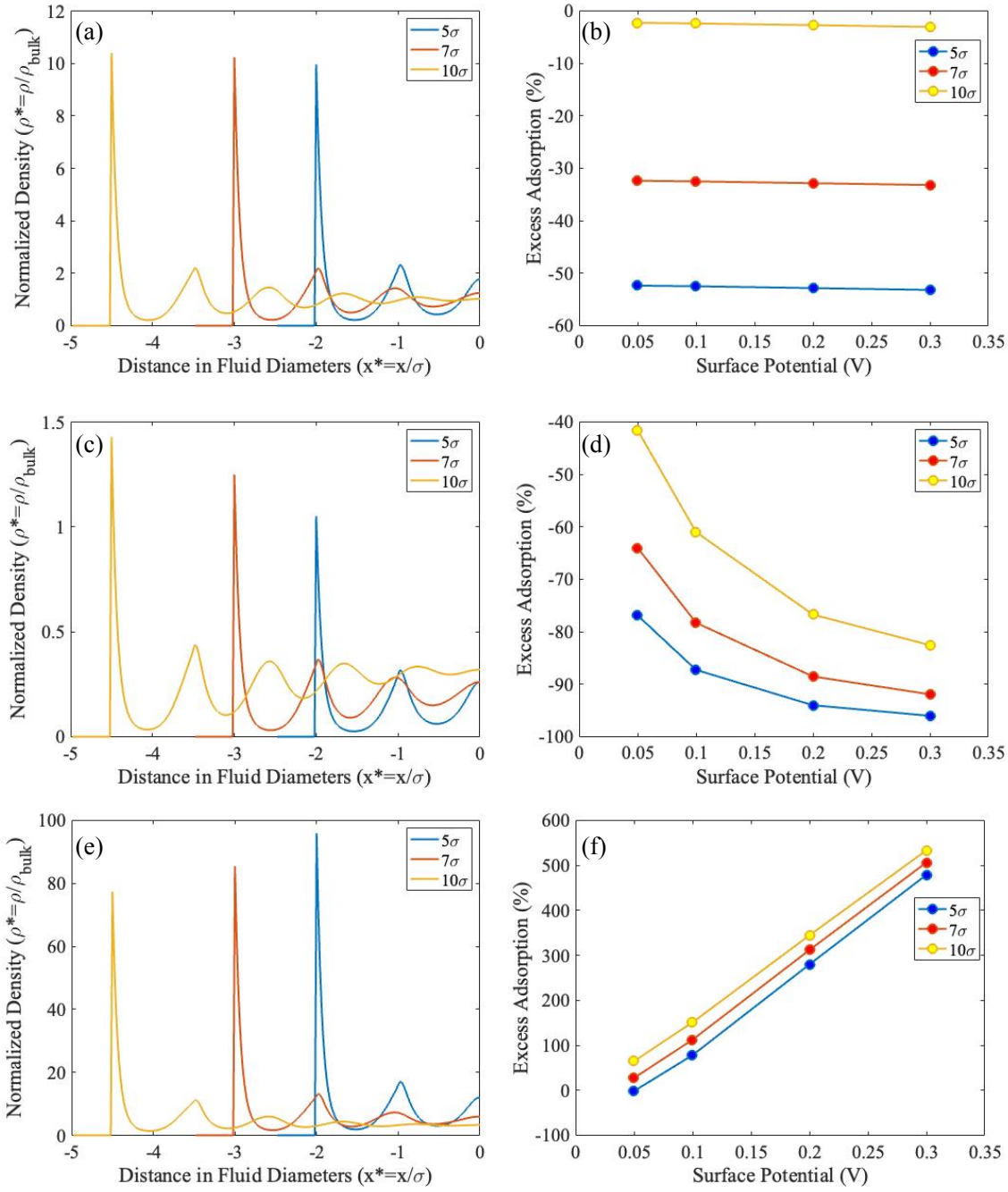

Figure 4-9: The density profiles for (a) solvent, (c) cations, and (e) anions with different slit widths. The corresponding net adsorptions for (b) solvent, (d) cations, and (f) anions are shown as well.

The first result shown is the normalized density for adsorbed species to the midplane and their subsequent excess adsorption for different slit widths. Figure 4-9(a) and 4-9(b) show that the first layer of adsorbed dipoles and cations decrease with decreasing slit widths. The excess adsorption of solvent decreases from -2.2% for the base case to -50% in the most nanoconfined slit. In contrast, the first layer of adsorbed anions actually increases. In contrast to this result, the total excess adsorption of all species decreases monotonically with decreasing slit capacitor. This result shows that steric repulsions dominate overall adsorption in extremely small nanoconfined pores.

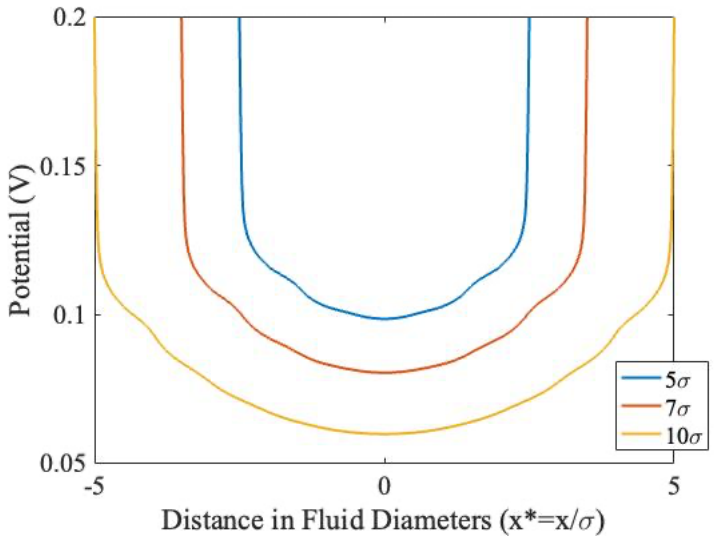

Figure 4-10: The electrostatic potential for different slit pore widths as a function of distance.

We can further analyze this behavior by analyzing the electrostatic potential within the confined geometry. Figure 4-10 shows the potential field for different slit capacitor lengths. Overall, all potential fields display similar shapes for different slit lengths. The curves follow a U shape with some inhomogeneities due to the characteristic density profiles from steric repulsions. The potential curves also display the expected trend of increasing midplane potentials with decreasing slit capacitor length due to overlapping double layer effects. This result confirms that the electrostatic interactions is favorable for anionic adsorption in more confined geometry; however, the slit wall steric repulsions dominate and lead to overall less adsorption.

Chapter 5: Conclusion and Recommendations

5.1 Summary of Work

In this work, we have identified common macroscopic theories used to understand electrolyte and dielectric behaviors at charged interfaces. The strong interest in manipulating double layer thermodynamics and applications of nanoporous electrodes have led to a desire to better understand the structure of electrolytes in nanopores. Solvent interactions and nanoconfinement effects are expected to play active roles in determining the double layer's thermodynamics. Computational work can play a critical role in filling this gap due to its ability to simulate molecular interactions and reorganizations from charged interfaces.

This work presented a c-DFT model capable of modeling inhomogeneous electrolytes in nanopores with explicit consideration for solvent interactions. This model used the dipolar Poisson-Boltzmann equation to mean-field electrostatic interactions between point dipoles and point ions. Steric repulsions are modeled using the Rosenfeld functional which is known to be able to accurately model hard sphere fluids in the low density regime. This model was used to simulate to structure of electrolytes in a symmetric surface potential nanopore using a simplified one-dimensional geometry. The surface potential, dipolar moment, temperature, and slit pore widths were varied to study their effects on structure and total excess adsorption.

This analysis showed that confinement has the largest effect on the excess adsorption for solvent and cations whereas surface potential has the largest effect on the anion adsorption. In the first layer of adsorbed solvent, the characteristic peak of solvent is primarily influenced by the steric repulsions from the densely adsorbed anions as opposed to electrostatic attractions. Furthermore, mean-field electrostatics do not predict a strongly aligned first layer of adsorbed solvent with the average angle only increasing by about 10^{o}. More investigations will be needed to understand if this is due to the negligence of correlation effects.

The current implementation also displayed many interesting effects due to overlapping double layers from the nanoconfined geometries. The overlapping double layers lead to midplane potentials that are nonzero and enhances adsorption of anions in the total domain. Larger confinements generally lead to increases in the midplane potential as well as the density of the first adsorbed layer of anions.

5.2 Future Work

A key component missing in this model is the effect of correlations in electrostatic interactions. Ion-ion correlations, ion-dipoles correlations, and dipole-dipole correlations can play significant roles in the structures that are not captured in the mean field dipolar Poisson-Boltzmann equation. It has been shown in the introduction and discussions that mean field dipolar electrostatics alone cannot capture all of the properties of strongly interacting liquids such as water. As seen in Chapter 1, the effects of local correlations play a strong role on the dielectric properties of water as predicted by Kirkwood's model. As a result, the first step to improving this method would be to include electrostatic correlation effects into the calculations.

Secondly, the Rosenfeld functional is known to be accurate for describing low density hard sphere fluids; however, it tends to overestimate the pressure at higher densities due to inaccuracies with SPT. It can be seen that the densities in the first layer of adsorbed fluids is very high for both anions and water in the symmetric case. A more accurate reference fluid, such as the White-Bear version Mark II fundamental measure theory, can lead to better predictions on the hard sphere repulsions in this region.

Thirdly, the implementation of specific chemical interactions into the functional can lead to interesting results that are more comparable with experiments. Currently, all electrolyte components have the same diameters. This leads to all the density profile peaks and troughs for all three electrolyte components to be in phase. It would be more interesting to consider size effects on how double layers can form close to charged interfaces. Mean-field Lennard-Jones attraction can also be added to simulate van der Waals interactions characteristic of each component.

Work Cited

[1] R. Roth and S. Dietrich, "Binary hard-sphere fluids near a hard wall," *Phys. Rev. E - Stat. Physics, Plasmas, Fluids, Relat. Interdiscip. Top.*, vol. 62, no. 5, pp. 6926–6936, 2000, doi: 10.1103/PhysRevE.62.6926.

[2] C. G. Malmberg and A. A. Maryott, "Dielectric constant of water from 0 to 100 C," *J. Res. Natl. Bur. Stand. (1934).*, vol. 56, no. 1, pp. 1–8, 1956, doi: 10.6028/jres.056.001.

[3] A. Härtel, M. Janssen, D. Weingarth, V. Presser, and R. Van Roij, "Heat-to-current conversion of low-grade heat from a thermocapacitive cycle by supercapacitors," *Energy Environ. Sci.*, vol. 8, no. 8, pp. 2396–2401, 2015, doi: 10.1039/c5ee01192b.

[4] X. Wang and S. P. Feng, "Thermal Capacitive Electrochemical Cycle on Carbon-Based Supercapacitor for Converting Low-grade Heat to Electricity," *Front. Mech. Eng.*, vol. 3, no. November, pp. 1–7, 2017, doi: 10.3389/fmech.2017.00020.

[5] F. Fahrenberger, Z. Xu, and C. Holm, "Simulation of electric double layers around charged colloids in aqueous solution of variable permittivity," *J. Chem. Phys.*, vol. 141, no. 6, pp. 1–10, 2014, doi: 10.1063/1.4892413.

[6] P. Attard, "Recent advances in the electric double layer in colloid science," *Curr. Opin. Colloid Interface Sci.*, vol. 6, no. 4, pp. 366–371, 2001, doi: 10.1016/S1359-0294(01)00102-9.

[7] W. Diao *et al.*, "Reversibly highly stretchable and self-healable zwitterion-containing polyelectrolyte hydrogel with high ionic conductivity for high-performance flexible and cold-resistant supercapacitor," *J. Appl. Polym. Sci.*, vol. 137, no. 34, pp. 1–14, 2020, doi: 10.1002/app.48995.

[8] X. Wang, K. Liu, and J. Wu, "Demystifying the Stern layer at a metal-electrolyte interface: Local dielectric constant, specific ion adsorption, and partial charge transfer," *J. Chem. Phys.*, vol. 154, no. 12, pp. 1–9, 2021, doi: 10.1063/5.0043963.

[9] B. E. Conway, *Electrochemical Capacitors Based on Pseudocapacitance*. 1999.

[10] A. Härtel, M. Janssen, S. Samin, and R. van Roij, "Fundamental measure theory for the electric double layer: implications for blue-energy harvesting and water desalination," *J. Phys. Condens. Matter*, vol. 27, no. 194129, pp. 1–12, 2015.

[11] M. Janssen, E. Griffioen, P. M. Biesheuvel, R. Van Roij, and B. Erné, "Coulometry and Calorimetry of Electric Double Layer Formation in Porous Electrodes," *Phys. Rev. Lett.*, vol. 119, no. 16, pp. 1–5, 2017, doi: 10.1103/PhysRevLett.119.166002.

[12] J. Theodoor and G. Overbeek, "The role of energy and entropy in the electrical double layer," *Colloids and Surfaces*, vol. 51, pp. 61–75, 1990.

[13] Z. Liu *et al.*, "Three-dimensional ordered porous electrode materials for electrochemical energy storage," *NPG Asia Mater.*, vol. 11, no. 1, 2019, doi: 10.1038/s41427-019-0112-3.

[14] Z. X. Luo, Y. Z. Xing, Y. C. Ling, A. Kleinhammes, and Y. Wu, "Electroneutrality breakdown and specific ion effects in nanoconfined aqueous electrolytes observed by NMR," *Nat. Commun.*, vol. 6, 2015, doi: 10.1038/ncomms7358.

[15] A. Levy, J. P. de Souza, and M. Z. Bazant, “Breakdown of electroneutrality in nanopores,” *J. Colloid Interface Sci.*, vol. 579, pp. 162–176, 2020, doi: 10.1016/j.jcis.2020.05.109.

[16] P. Debye, “Some results of kinetic theory of insulators,” *Phys. Zeitschrift*, vol. 13, pp. 97–100, 1912.

[17] L. Onsager, “Electric moments of molecules in liquids,” *J. Am. Chem.Soc.*, vol. 58, no. 8, pp. 1486–1493, 1936.

[18] J. G. Kirkwood, “On the theory of dielectric polarization,” *J. Chem.Phys.*, vol. 4, no. 592, 1936.

[19] G. Oster and J. G. Kirkwod, “The influence of hindered molecular rotation on the dielectric constant of water, alcohols, and other polar liquids,” *J. Chem.Phys.*, vol. 11, pp. 175–178, 1943.

[20] J. W. Lee, R. H. Nilson, J. A. Templeton, S. K. Griffiths, A. Kung, and B. M. Wong, “Comparison of molecular dynamics with classical density functional and Poisson-Boltzmann theories of the electric double layer in nanochannels,” *J. Chem. Theory Comput.*, vol. 8, no. 6, pp. 2012–2022, 2012, doi: 10.1021/ct3001156.

[21] A. Hartel, “Structure of electric double layers in capacitive systems and to what extent (classical) density functional theory describes it,” *J. Phys. Condens. Matter*, vol. 29, no. 42, 2017, doi: 10.1088/1361-648X/aa8342.

[22] G. Jiang, C. Cheng, D. Li, and J. Z. Liu, “Molecular dynamics simulations of the electric double layer capacitance of graphene electrodes in mono-valent aqueous electrolytes,” *Nano Res.*, vol. 9, no. 1, pp. 174–186, 2016, doi: 10.1007/s12274-015-0978-5.

[23] H. von Helmholtz, “Studien über elektrische Grenzscichten,” *Ann. der Phys. Und Chemie*, vol. 243, no. 7, pp. 337–382, 1879.

[24] L. G. Gouy, “Sur la constitution de la charge électrique à la surface d’un électrolyte,” *J. Phys. Theor. Appl.*, vol. 9, no. 1, pp. 457–468, 1910.

[25] D. L. Chapman, “A contribution to the theory of electrocapillarity,” *Philos. Mag.*, vol. 25, no. 148, pp. 475–481, 1913.

[26] O. Stern, “Zur theory der elektrolytischen doppelschicht,” *Z. Electrochem.*, vol. 30, no. 508, 1924.

[27] P. Debye and E. Hückel, “The theory of electrolytes. I. Freezing point depression and related pheonmena,” *Phys. Zeitschrift*, vol. 24, pp. 185–206, 1923.

[28] J. O. Bockris, M. A. V. Devanathan, and K. Müller, “On the structure of charged interfaces,” *Proc. R. Soc. Lond. A*, vol. 274, pp. 55–59, 1963, doi: 10.1016/0250-6874(81)80007-8.

[29] S. L. Marshall and B. E. Conway, “Analysis of molecular polarization and interaction in adsorbed monolayers at electrodes: Part 2. Surface solvation energy of adsorbed charges,” *J. Electroanal. Chem.*, vol. 337, no. 1–2, pp. 19–43, 1992, doi: 10.1016/0022-0728(92)80528-C.

[30] S. L. Marshall and B. E. Conway, “Analysis of molecular polarization and interaction in adsorbed monolayers at electrodes: Part 1. Interaction between adsorbed dipoles,” *J. Electroanal. Chem.*, vol. 337, no. 1–2, pp. 1–18, 1992, doi: 10.1016/0022-0728(92)80528-C.

[31] R. Evans, *Fundamentals of Inhomogeneous Fluids*, vol. Ch. 3 Dens. 1992.

[32] S. M. Tschopp, H. D. Vuijk, A. Sharma, and J. M. Brader, “Mean-field theory of inhomogeneous fluids,” *Phys. Rev. E*, vol. 102, no. 4, p. 42140, 2020, doi: 10.1103/PhysRevE.102.042140.

[33] D. E. Sullivan, “Statistical mechanics of nonuniform fluid with long-range attractoins,” *Phys. Rev. A*, vol. 25, no. 3, pp. 1669–1682, 1982.

[34] J. Liu, X. He, J. Z. H. Zhang, and L. W. Qi, “Hydrogen-bond structure dynamics in bulk water: Insights from: Ab initio simulations with coupled cluster theory,” *Chem. Sci.*, vol. 9, no. 8, pp. 2065–2073, 2018, doi: 10.1039/c7sc04205a.

[35] M. S. Wertheim, “Fluids with highly directional attractive forces. I. Statistical thermodynamics,” *J. Stat. Phys.*, vol. 35, no. 1–2, pp. 19–34, 1984, doi: 10.1007/BF01017362.

[36] M. S. Wertheim, “Fluids with Highly Directional Attractive Forces. II. Thermodynamic Perturbation Theory and Integral Equations,” *J. Stat. Phys.*, vol. 35, no. 1–2, pp. 35–47, 1984, doi: 10.1007/BF01127722.

[37] M. S. Wertheim, “Fluids with Highly Directional Attractive Forces. III. Multiple Attraction Sites,” *J. Stat. Phys.*, vol. 42, no. 3–4, pp. 459–476, 1986.

[38] M. S. Wertheim, “Fluids with highly directional attractive forces. IV. Equilibrium polymerization,” *J. Stat. Phys.*, vol. 42, no. 3–4, pp. 477–492, 1986, doi: 10.1007/BF01127722.

[39] A. Gil-Villegas, A. Galindo, P. J. Whitehead, S. J. Mills, G. Jackson, and A. N. Burgess, “Statistical associating fluid theory for chain molecules with attractive potentials of variable range,” *J. Chem. Phys.*, vol. 106, no. 10, pp. 4168–4186, 1997, doi: 10.1063/1.473101.

[40] W. G. Chapman, K. E. Gubbins, G. Jackson, and M. Radosz, “SAFT: Equation-of-state solution model for associating fluids,” *Fluid Phase Equilib.*, vol. 52, no. C, pp. 31–38, 1989, doi: 10.1016/0378-3812(89)80308-5.

[41] C. J. Segura, W. G. Chapman, and K. Shukla, “Associating fluids with four bonding sites against a hard wall: Density functional theory,” *Mol. Phys.*, vol. 90, no. 5, pp. 759–771, 1997, doi: 10.1080/002689797172110.

[42] A. Bymaster and W. G. Chapman, “An iSAFT density functional theory for associating polyatomic molecules,” *J. Phys. Chem. B*, vol. 114, no. 38, pp. 12298–12307, 2010, doi: 10.1021/jp102677m.

[43] J. Hughes, E. J. Krebs, and D. Roundy, “A classical density-functional theory for describing water interfaces,” *J. Chem. Phys.*, vol. 138, no. 2, 2013, doi: 10.1063/1.4774155.

[44] G. N. I. Clark, A. J. Haslam, A. Galindo, and G. Jackson, "Developing optimal Wertheim-like models of water for use in Statistical Associating Fluid Theory (SAFT) and related approaches," *Mol. Phys.*, vol. 104, no. 22–24, pp. 3561–3581, 2006, doi: 10.1080/00268970601081475.

[45] T. B. Peery and G. T. Evans, "Association in a four-coordinated, water-like fluid," *J. Chem. Phys.*, vol. 118, no. 5, pp. 2286–2300, 2003, doi: 10.1063/1.1534575.

[46] F. Llovell, N. Mac Dowell, F. J. Blas, A. Galindo, and G. Jackson, "Application of the SAFT-VR density functional theory to the prediction of the interfacial properties of mixtures of relevance to reservoir engineering," *Fluid Phase Equilib.*, vol. 336, pp. 137–150, 2012, doi: 10.1016/j.fluid.2012.07.033.

[47] K. Gong, B. D. Marshall, and W. G. Chapman, "Modeling lower critical solution temperature behavior of associating polymer brushes with classical density functional theory," *J. Chem. Phys.*, vol. 139, no. 9, 2013, doi: 10.1063/1.4819957.

[48] E. K. Karakatsani, T. Spyriouni, and I. G. Economou, "Extended statistical associating fluid theory (SAFT) equations of state for dipolar fluids," *AIChE J.*, vol. 51, no. 8, pp. 2328–2342, 2005, doi: 10.1002/aic.10473.

[49] J. M. Walsh, H. J. R. Guedes, and K. E. Gubbins, "Physical theory for fluids of small associating molecules," *J. Phys. Chem.*, vol. 96, no. 26, pp. 10995–11004, 1992, doi: 10.1021/j100205a071.

[50] Y. A. Budkov and A. L. Kolesnikov, "Nonlocal density functional theory of water taking into account many-body dipole correlations: Binodal and surface tension of 'liquid-vapour' interface," *J. Phys. Condens. Matter*, vol. 32, no. 365001, pp. 1–13, 2020, doi: 10.1088/1361-648X/ab884a.

[51] R. J. Sadus, "Molecular simulation of the vapour-liquid equilibria of pure fluids and binary mixtures containing dipolar components: The effect of Keesom interactions," *Mol. Phys.*, vol. 87, no. 5, pp. 979–990, 1996, doi: 10.1080/00268979600100661.

[52] G. Jeanmairet, M. Levesque, R. Vuilleumier, and D. Borgis, "Molecular density functional theory of water including density-polarization coupling," *J. Phys. Chem. L*, vol. 4, no. 4, pp. 619–624, 2013, doi: dx.doi.org/10.1021/jz301956b.

[53] S. L. Carnie, D. Y. C. Chan, D. J. Mitchell, and B. W. Ninham, "The structure of electrolytes at charged surfaces: The primitive model," *J. Chem. Phys.*, vol. 74, no. 2, pp. 1472–1478, 1981, doi: 10.1063/1.441161.

[54] J. S. Høye and G. Stell, "Mean spherical approximation (MSA) for a simple model of electrolytes. I. Theoretical foundations and thermodynamics," *J. Chem. Phys.*, vol. 88, no. 9, pp. 5790–5797, 1988, doi: 10.1063/1.455278.

[55] M. S. Wertheim, "Exact solution of the mean spherical model for fluids of hard spheres with permanent electric dipole moments," *J. Chem. Phys.*, vol. 55, no. 9, pp. 4291–4298, 1971, doi: 10.1063/1.1676751.

[56] R. Ramirez and D. Borgis, "Density functional theory of solvation and its relation to implicit solvent models," *J. Phys. Chem. B*, vol. 109, no. 14, pp. 6754–6763, 2005, doi: 10.1021/jp045453v.

[57] V. Warshavsky and M. Marucho, "Polar-solvation classical density-functional theory for

electrolyte aqueous solutions near a wall," *Phys. Rev. E*, vol. 93, no. 4, pp. 1–19, 2016, doi: 10.1103/PhysRevE.93.042607.

[58] S. Y. Mashayak and N. R. Aluru, "Langevin-Poisson-EQT: A dipolar solvent based quasi-continuum approach for electric double layers," *J. Chem. Phys.*, vol. 146, no. 4, 2017, doi: 10.1063/1.4973934.

[59] J.-P. Hansen and I. R. McDonald, *Theory of Simple Liquids: with Applications to Soft Matter*, Fourth Ed. Oxford: Academic Press, 2013.

[60] Y. Rosenfeld, "Free-energy model for the inhomogeneous hard-sphere fluid mixture and density-functional theory of freezing," *Phys. Rev. Lett.*, vol. 63, no. 9, pp. 980–983, 1989, doi: 10.1103/PhysRevLett.63.980.

[61] A. Abrashkin, D. Andelman, and H. Orland, "Dipolar Poisson-Boltzmann equation: Ions and dipoles close to charge interfaces," *Phys. Rev. Lett.*, vol. 99, no. 7, pp. 1–4, 2007, doi: 10.1103/PhysRevLett.99.077801.

[62] D. Frydel, "Mean Field Electrostatics Beyond the Point Charge Description," *Adv. Chem. Phys.*, vol. 160, no. 1, pp. 209–260, 2016, doi: 10.1002/9781119165156.ch4.

[63] P. Koehl and M. Delarue, "AQUASOL: An efficient solver for the dipolar Poisson-Boltzmann-Langevin equation," *J. Chem. Phys.*, vol. 132, no. 6, pp. 1–16, 2010, doi: 10.1063/1.3298862.

[64] A. V. Gubskaya and P. G. Kusalik, "The total molecular dipole moment for liquid water," *J. Chem. Phys.*, vol. 117, no. 11, pp. 5290–5302, 2002, doi: 10.1063/1.1501122.

Appendix A. Rosenfeld Functional One Body Correlation Terms

A brief derivation is given here to show the functional form of the Rosenfeld functional's one body direct correlation terms for use in the one-dimensional case and one component for notation simplicity. Extension to a mixture is simple by considering the summations in the weighting functions. Eq. 2.3.17 is commonly decomposed into three components.

$$\Phi = \Phi_1 + \Phi_2 + \Phi_3 \qquad \text{Eq. A.1}$$

$$\Phi_1 = -\eta_{(0)} \ln\left(1 - \eta_{(3)}\right) \qquad \text{Eq. A.2}$$

$$\Phi_2 = \frac{\eta_{(1)}\eta_{(2)} - \underline{\eta}_{(1)} \cdot \underline{\eta}_{(2)}}{1 - \eta_{(3)}} \qquad \text{Eq. A.3}$$

$$\Phi_3 = \frac{\eta_{(2)}^3 - 3\eta_{(2)}\underline{\eta}_{(2)} \cdot \underline{\eta}_{(2)}}{24\pi\left(1 - \eta_{(3)}\right)^2} \qquad \text{Eq. A.4}$$

The partial derivatives of the Rosenfeld functional with respect to each weighted density is then calculated below.

$$\frac{\partial \Phi}{\partial \eta_{(0)}} = \frac{\partial \Phi_1}{\partial \eta_{(0)}} = -\ln(1 - \eta_3) \qquad \text{Eq. A.5}$$

$$\frac{\partial \Phi}{\partial \eta_{(1)}} = \frac{\partial \Phi_2}{\partial \eta_{(1)}} = \frac{\eta_{(2)}}{1 - \eta_{(3)}} \qquad \text{Eq. A.6}$$

$$\frac{\partial \Phi}{\partial \eta_{(2)}} = \frac{\partial \Phi_2}{\partial \eta_{(2)}} + \frac{\partial \Phi_3}{\partial \eta_{(2)}} = \frac{\eta_{(1)}}{1 - \eta_{(3)}} + \frac{\left(\eta_{(2)}^2 - \underline{\eta}_{(2)} \cdot \underline{\eta}_{(2)}\right)}{8\pi\left(1 - \eta_{(3)}\right)^2} \qquad \text{Eq. A.7}$$

$$\frac{\partial \Phi}{\partial \eta_{(3)}} = \frac{\partial \Phi_1}{\partial \eta_{(3)}} + \frac{\partial \Phi_2}{\partial \eta_{(3)}} + \frac{\partial \Phi_3}{\partial \eta_{(3)}}$$

$$= \frac{\eta_{(0)}}{1 - \eta_{(3)}} + \frac{\eta_{(1)}\eta_{(2)} - \underline{\eta}_{(1)} \cdot \underline{\eta}_{(2)}}{\left(1 - \eta_{(3)}\right)^2} + \frac{\eta_{(2)}^3 - 3\eta_{(2)}\eta_{(2)} \cdot \underline{\eta}_{(2)}}{12\pi\left(1 - \eta_{(3)}\right)^3} \qquad \text{Eq. A.8}$$

$$\frac{\partial \Phi}{\partial \underline{\eta}_{(1)}} = \frac{\partial \Phi_2}{\partial \underline{\eta}_{(1)}} = \frac{-\underline{\eta}_{(2)}}{1 - \eta_{(3)}} \qquad \text{Eq. A.9}$$

$$\frac{\partial \Phi}{\partial \underline{\eta}_{(2)}} = \frac{\partial \Phi_2}{\partial \underline{\eta}_{(2)}} + \frac{\partial \Phi_3}{\partial \underline{\eta}_{(2)}}$$
$$= \frac{-\underline{\eta}_{(1)}}{1-\eta_{(3)}} - \frac{\eta_{(2)}\underline{\eta}_{(2)}}{4\pi\left(1-\eta_{(3)}\right)^2} \qquad \text{Eq. A.10}$$

Finally, the partial derivatives of each weighted density $\eta_{(k)}$ with respect to the density of each component is simply the integral of the weighting functions given in Eq. 2.3.6 to 2.2.11. The hard sphere one-body direct correlation factor can then be calculated by plugging in the respective values to Eq. 2.2.16.

Appendix B. Derivation of Dipolar Poisson-Boltzmann Equation

Here the derivation for the dipolar Poisson-Boltzmann equation will be briefly illustrated using a method similar to c-DFT. In Eq 2.4.1, it is recognized that the first term is equal to the total charge density due to dipolar species. Using the definition of the polarization density, it is recognized that this term is equal to the divergence of the polarization density.

$$-\sum_{i=1}^{M}\int d\underline{p}_D\left[\underline{p}_D\cdot\nabla\rho_D\left(\underline{r},\underline{n}\right)\right]=\underline{\nabla}\cdot\underline{P}(\underline{r}) \qquad \text{Eq. B.1}$$

It is then recognized that the polarization vector is aligned with the electric field, and can be restated using the electric field vector.

$$\underline{P}=P\left(\frac{\underline{\nabla}\phi}{\phi}\right) \qquad \text{Eq. B.2}$$

As a result, the magnitude of the polarization vector is related to the vector sum of all dipole moments aligned with the electric field per unit volume.

$$P=\sum\frac{p_D cos\theta}{V} \qquad \text{Eq. B.3}$$

The summation is then converted into an integral over the solid angle normalized to the solid angle.

$$P=\frac{\int_0^{\pi}\rho_D\left(\underline{r},\theta\right)p_D 2\pi cos\theta sin\theta d\theta}{4\pi} \qquad \text{Eq. B.4}$$

The dipolar density can be re-written to include only the effects of electrostatic potential energy.

$$\rho_D\left(\underline{r},\theta\right)=\rho_{D,bulk}\exp(\beta p_D|\nabla\phi|cos\theta) \qquad \text{Eq. B.5}$$

Plugging Eq. B.5 into Eq. B.3 and integrating gives

$$P=p_D\left(\frac{\rho_{D,bulk}\sinh(\beta p_D|\nabla\phi|)}{\beta p_D|\nabla\phi|}\right)\left(\coth(\beta p_D|\nabla\phi|)-\frac{1}{\beta p_D|\nabla\phi|}\right) \qquad \text{Eq. B.6}$$

where the first term brackets corresponds to the number density of dipoles due to an external electric field and the second term is the Langevin function. The first term is then grouped into a general ρ_D term to couple the dipolar density with other potential energy terms in the c-DFT iteration scheme. Eq. B.6 can then be combined with Eq. B.1 and Eq. 2.4.1 form the dipolar Poisson-Boltzmann equation modified for c-DFT calculations.

Appendix C. Derivation of Jacobian in Dipolar Poisson-Boltzmann Solver

This section will briefly describe the full derivations used for the Jacobian calculation using the finite volume method. Taking Eq. 3.3.7, the elements of vector B for position $i-1$, i, and $i+1$ can be written.

$$\underline{B}_{i,i-1} = \frac{\partial \underline{F}_i}{\partial \phi_{i-1}} = -\frac{\partial \epsilon_{r,i-\frac{1}{2}}}{\partial \phi_{i-1}}\phi_{i-1} + \frac{\partial \epsilon_{r,i-\frac{1}{2}}}{\partial \phi_{i-1}}\phi_i \quad \text{Eq. C.1}$$

$$\underline{B}_{i,i} = \frac{\partial \underline{F}_i}{\partial \phi_i} = \frac{\partial \epsilon_{r,i-\frac{1}{2}}}{\partial \phi_i}\phi_{i-1} - \left(\frac{\partial \epsilon_{r,i-\frac{1}{2}}}{\partial \phi_i} + \frac{\partial \epsilon_{r,i+\frac{1}{2}}}{\partial \phi_i}\right)\phi_i + \frac{\partial \epsilon_{r,i+\frac{1}{2}}}{\partial \phi_i}\phi_{i+1} \quad \text{Eq. C.2}$$

$$\underline{B}_{i,i+1} = \frac{\partial \underline{F}_i}{\partial \phi_{i+1}} = -\frac{\partial \epsilon_{r,i+\frac{1}{2}}}{\partial \phi_{i+1}}\phi_{i+1} + \frac{\partial \epsilon_{r,i+\frac{1}{2}}}{\partial \phi_{i+1}}\phi_i \quad \text{Eq. C.3}$$

The partial derivatives for the relative permittivity with respect to the potential at each point can then be written by using Eq. 3.3.12 and using chain rule with respect to the potential.

$$\frac{\partial \epsilon_r}{\partial \nabla\phi} = \begin{cases} \frac{\rho_D p_D}{\epsilon_0}\left(\frac{\nabla\phi}{\beta p_D |\nabla\phi|^4} - \frac{\beta p_D \nabla\phi \,\mathrm{csch}^2(\beta p_D|\nabla\phi|)}{|\nabla\phi|^2} - \frac{\nabla\phi \coth(\beta p_D|\nabla\phi|)}{|\nabla\phi|^3} - \frac{\nabla\phi}{\beta p_D|\nabla\phi|^4}\right) & Z > 10^{-4} \\ \frac{\rho_D p_D}{\epsilon_0}\left[-\frac{2}{45}(\beta p_D)^3|\nabla\phi| + \frac{8}{945}(\beta p_D)^5|\nabla\phi|^3 - \frac{6}{4725}(\beta p_D)^7|\nabla\phi|^5\right] & Z \le 10^{-4} \end{cases} \quad \text{Eq. C.4}$$

$$\frac{\partial \nabla\phi}{\partial \phi_i} = \frac{\partial\left[\frac{(\phi_{i+1}-\phi_i)}{dx}\right]}{\partial \phi_i} = -\frac{1}{dx} \quad \text{Eq. C.5}$$

$$\frac{\partial \nabla\phi}{\partial \phi_{i+1}} = \frac{\partial\left[\frac{(\phi_{i+1}-\phi_i)}{dx}\right]}{\partial \phi_i} = \frac{1}{dx} \quad \text{Eq. C.6}$$

Plugging Eq. C.4-C.6 into Eq C.1-C.3 will construct the matrix for the partial derivative of the $\underline{\underline{A}}$ matrix with respect to the potential field. The partial derivative of C is calculated similarly using Eq. C.1-C.6.